Power Electronic Systems
Laboratory

IEEE Transactions On Industry Applications, Vol. 58, No. 4, pp. 5026-5041, August 2021

Beyond 50MHz Bandwidth Extension of Commercial DC-Current Measurement Sensors with Ultra-Compact PCB Integrated Pickup Coils

P. Niklaus,
D. Bortis,
J. W. Kolar

Eidgenössische Technische Hochschule Zürich
Swiss Federal Institute of Technology Zurich

This article has been accepted for publication in IEEE Transactions on Industry Applications. This is the author's version which has not been fully edited and content may change prior to final publication. Citation information: DOI 10.1109/TIA.2022.3164865

Beyond 50 MHz Bandwidth Extension of Commercial DC-Current Measurement Sensors with Ultra-Compact PCB Integrated Pickup Coils

Pascal S. Niklaus, *Student Member, IEEE,* Dominik Bortis, *Member, IEEE,* and Johann W. Kolar, *Fellow, IEEE*

***Abstract*—The control of very high switching frequency power electronic converter systems featuring latest generation wide bandgap (WBG) devices requires current measurements with a very high bandwidth (BW) to achieve high closed-loop control dynamics. One example is an ultra-high BW 4.8 MHz parallel-interleaved multi-level GaN inverter ac power source with a target large-signal output BW of 100 kHz. This work investigates the combination of commercially available low-frequency (LF) Hall-effect current sensors (BW$\approx$ 1 MHz) with suitable high-frequency (HF) sensors to extend the BW above 10 MHz, i.e., enough to measure the HF inductor current. Based on a conventional PCB integrated Rogowski coil, for the HF sensor three improved pickup coil (PUC) geometries based on proposals in the literature are investigated. The LF and HF sensor signals are combined with a precision fully-differential combiner circuit. Design guidelines for the HF sensors as well as the combiner circuit are presented and thereby the influence of mismatches and tolerances is examined. The performance of the proposed HF sensors is experimentally verified and compared to previous solutions based on galvanically isolated inductor voltage sensing (IVS) and a current transformer (CT). The PUCs reach a BW $>$ 50 MHz, which is an improvement by more than a factor of 50 compared to the fastest available Hall sensor. Furthermore, it is proven that all investigated sensors are capable to accurately measure the triangular inductor current ripple in a hardware prototype of the aforementioned ac power source. In a final step, the influence of common-mode (CM) disturbances originating from fast $\mathrm{dv/dt}$ switching transients on the sensor performance is analyzed. The presented current sensors achieve a CM Rejection Ratio (CMRR) of almost 100 dB.**

***Index Terms*—High-Frequency Current Measurement, Hall Sensor, Rogowski Coil, Current Transformer, Inverter, Pickup Coil, Wide Bandgap Semiconductors, Multi-Level Converter, Ultra-High Bandwidth DC/AC Converter**

I. Introduction

MODERN power electronic converter systems typically use latest wide bandgap (WBG) power semiconductors to allow higher switching frequencies (in the MHz-range), which in turn results in very power-dense system realizations. Besides a higher power density, MHz-range switching frequencies enable the realization of highly dynamic converter systems such as the GaN-based phase-modular 10 kW (per phase) AC power source with 100 kHz large-signal output bandwidth (BW) and an effective switching frequency of $f_{\mathrm{sw,eff}} = 4.8\,\mathrm{MHz}$ described in [1]. **Fig. 1 (a)** shows the proposed converter topology, a three-level ($N_{\mathrm{ser}} = 3$) triple-interleaved ($N_{\mathrm{par}} = 3$) flying capacitor converter (*3L3*) with the main specifications listed in **Fig. 1 (b)**. Each switching cell (two switches plus a flying capacitor) switches with 800 kHz, which results in a current ripple with a frequency of $f_{\mathrm{iLpp}} = 1.6\,\mathrm{MHz}$ in each of the three branch inductors L_{br}. The parallel-interleaved operation and the subsequent summation of the three inductor currents $i_{\mathrm{L},1\ldots3}$ at the output filter capacitor node results in the effective switching frequency of 4.8 MHz. For closed-loop operation with up to 100 kHz large signal output BW a cascaded control scheme with a very fast inner current controller and outer voltage controller including several feedforward paths turned out to be the most promising approach [2]. Wideband current and voltage measurements are required for proper operation of these fast controllers. The former is depicted in **Fig. 1 (a)** and is typically more challenging to realize in practice compared to voltage measurements, since most state-of-the-art current measurement principles are covering either DC and low frequencies (LF) $<$ 1 MHz or high frequencies (HF) but not DC. The following requirements are

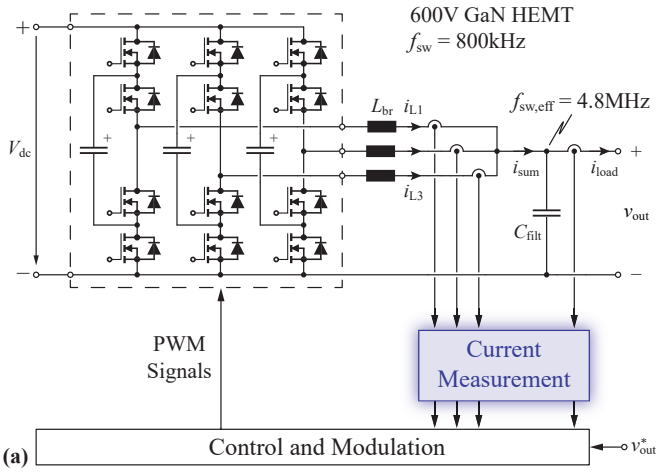

(a)

Parameter		Value
Peak Output Voltage per Phase	$V_{\mathrm{out,pk}}$	0 ... 350 V
Output Frequency	f_{out}	DC ... 100 kHz
Output Power per Phase	P_{out}	0 ... 10 kW
DC Link Voltage	V_{dc}	800 V
Effective Switching Frequency	$f_{\mathrm{sw,eff}}$	4.8 MHz

(b)

Fig. 1. (a) System overview of the 100 kHz large signal output voltage control bandwidth (BW) power amplifier realized as three-level triple interleaved (*3L3*) converter with GaN switches. **(b)** The main system specifications.

This paper was presented in part at the 2021 IEEE Applied Power Electronic Conference and Exposition (APEC), Phoenix, USA, June 2021.
(Corresponding Author: Pascal S. Niklaus)

P. S. Niklaus, D. Bortis and J. W. Kolar are with the Power Electronic Systems Laboratory, Swiss Federal Institute of Technology, Zurich 8092, Switzerland (e-mail: niklaus@lem.ee.ethz.ch; antivachis@lem.ee.ethz.ch; bortis@lem.ee.ethz.ch; kolar@lem.ee.ethz.ch).

This article has been accepted for publication in IEEE Transactions on Industry Applications. This is the author's version which has not been fully edited and content may change prior to final publication. Citation information: DOI 10.1109/TIA.2022.3164865

considered for the target current measurement:

- DC capable and $> 10\,\mathrm{MHz}$ BW to capture at least six harmonics (even and/or odd) of the $1.6\,\mathrm{MHz}$ triangular inductor currents,
- galvanic isolation to allow current measurements on a floating potential,
- no or very low added losses,
- measurement range of $\pm 40\,\mathrm{A}$ for the inductor current and $\pm 65\,\mathrm{A}$ for the output current with a sensitivity in the range of $15 - 30\,\mathrm{mV/A}$ to maximally utilize the full-scale voltage range of typical analog-to-digital converters (ADCs),
- high immunity to common-mode (CM) disturbances resulting from the high $\mathrm{d}v/\mathrm{d}t$ of WBG semiconductors,
- small form factor.
- Deviation of $< \pm 3\,\%$ over the frequency range (corresponds to $\pm 0.25\,\mathrm{dB}$ variation).

Generally, an accuracy in the range of several percent is considered sufficient for the current measurement, since it is part of the inner current control loop. The outer voltage control loop, which typically has integrating behavior [2], can still correct residual errors from the inner loop that are within the voltage controller bandwidth.

Most state-of-the-art commercial current sensors either rely on the Hall-effect [3], [4], feature a magneto-resistive element [5] or work based on the flux-gate principle [6]. They offer very high precision, adequate sensitivity, high CM immunity, galvanic isolation and they are DC capable. Common to all is, however, the fundamental disadvantage of limited BW in the range of only $500\,\mathrm{kHz}$ to $1\,\mathrm{MHz}$, which is at least one order of magnitude too low for the given application.

Although a commercial off-the-shelf solution would be desirable due to the ease of use and small form factor, unfortunately, no device that meets all the above requirements, particularly the BW, exists. To benefit from the aforementioned advantages of commercial sensors, an extension of the frequency range of a readily available commercial current sensor to make it suitable for the given application is required.

The combination of a LF and HF current sensor has been comprehensively studied in literature. A typical approach is to use a Hall element in a open-loop [7]–[9] or closed-loop [10]–[12] configuration to measure the remaining magnetic flux density in the core of a gapped current transformer (CT). In the former case, the LF Hall element voltage is directly added to the output of the current transformer, whereas in the latter case a compensator injects a current into the CT secondary winding to nullify the magnetic flux in the core. The closed-loop approach has the advantage of linearizing the Hall element's response but is fairly complex to realize. The common disadvantage of both approaches is the gap in the magnetic core to fit the Hall element, which complicates the manufacturing. Furthermore, there is a pronounced stray field in the vicinity of the air gap, which particularly for the open-loop configurations could distort the Hall element measurements due to parasitic voltage induction in the connecting leads [8], [10]. In [13], a Hall sensor and CT are operated independently of each other and combined using a dedicated combiner network. An alternative approach is presented in [14] where a Hall element in open-loop configuration is combined with a Rogowski coil [15]. The Rogowski coil measures the change in current and therefore needs a subsequent integration stage to obtain a signal that is proportional to the current [11], [16], [17]. This inherently limits the DC and LF response, which is added by the Hall element.

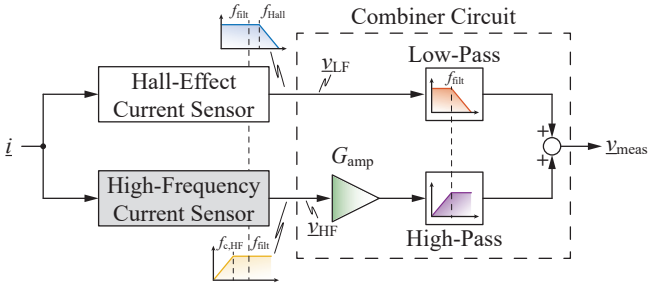

Fig. 2. Block diagram of the current measurement system including the combiner circuit proposed in [18].

Different possibilities to combine a LF Hall-effect and a HF current sensor have been previously analyzed and compared by the authors in [18] aiming for a BW extension of commercially available LF current sensors. This paper briefly summarizes the findings of [18] in **Section II** and extends it with an alternative approach for the combination presented in **Section III**, which simplifies the HF current sensor design. Thereby, very compact and highly linear PCB integrated Rogowski coils can be used. Then, **Section IV** presents three favorable PCB integrated realizations for the HF Rogowski coil to achieve the desired coupling with very compact sensors and compares them to the classical toroidal Rogowski coil realization. Afterwards, the performance is verified experimentally in **Section V** and in **Section VI** the immunity with respect to common-mode (CM) disturbances is analyzed. Finally, **Section VII** discusses the findings and compares them to results in literature before **Section VIII** concludes the paper.

II. HF Extension of LF Hall-effect Sensor

This section briefly summarizes the findings of [18] where a commercial fully integrated Hall-effect current sensor is combined with a suitable HF sensor using an analog combiner circuit.

A. Measurement System

Fig. 2 shows the block diagram of the initially proposed measurement system including the combiner circuit to combine the signal $\underline{v}_{\mathrm{LF}}$ of the LF Hall-effect sensor (Allegro ACS733 [4]) with its inherent low-pass characteristic (corner frequency f_{Hall}) with the signal $\underline{v}_{\mathrm{HF}}$ of the HF extension (cf. **Section II-B**), which has an intrinsic high-pass characteristic (corner frequency $f_{\mathrm{c,HF}}$). Please note, that $\underline{x}$ indicates a complex quantity with a magnitude and phase information. If both, the LF and HF sensor show an ideal first-order low-pass and high-pass response with $f_{\mathrm{Hall}} = f_{\mathrm{c,HF}}$, ideally, no combiner circuit would be required for a flat frequency response but the two signals could just be added. In practice, this is unfortunately not the case - particularly the Hall sensor frequency response deviates from a first-order low-pass response [4] - resulting in magnitude and phase errors. The combiner network therefore introduces an additional low-pass characteristic with corner frequency $f_{\mathrm{filt}} = \omega_{\mathrm{filt}}/(2\pi)$ for $\underline{v}_{\mathrm{LF}}$ and a high-pass characteristic with the same corner frequency

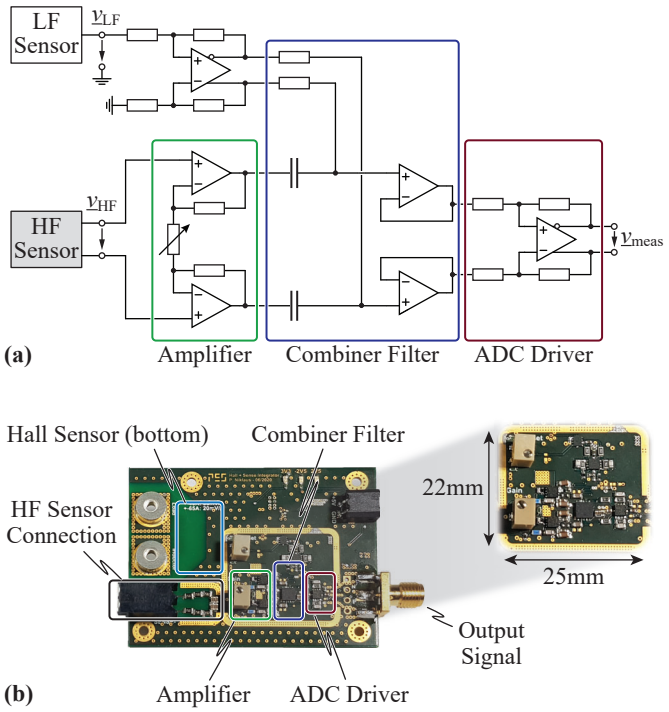

Fig. 3. **(a)** Simplified schematic of the fully differential combiner circuit of [18] and **(b)** picture of the realized hardware demonstrator for the performance evaluation. The individual circuit blocks are highlighted.

f_{filt} for $\underline{v}_{\mathrm{HF}}$ such that the summation of the two voltages equals

$$\underline{v}_{\mathrm{meas}} = \underline{v}_{\mathrm{LF}} \cdot \frac{1}{1 + s/\omega_{\mathrm{filt}}} + \underline{v}_{\mathrm{HF}} \cdot G_{\mathrm{amp}} \cdot \frac{s/\omega_{\mathrm{filt}}}{1 + s/\omega_{\mathrm{filt}}}. \quad (1)$$

For a flat frequency response in the transition range around f_{filt} a large overlap in the LF and HF sensor frequency response is therefore required ($f_{\mathrm{c,HF}} < f_{\mathrm{filt}} < f_{\mathrm{Hall}}$). This vanishes the influence of the inherent LF sensor low-pass and HF sensor high-pass characteristic and the transition is solely defined by the combiner network. With the Hall sensor frequency response taken from the datasheet [4] the HF sensor corner frequency and the combiner frequency have to be chosen lower than $f_{\mathrm{c,HF}} < 500\,\mathrm{Hz}$ and $f_{\mathrm{filt}} < 19\,\mathrm{kHz}$, respectively, to keep the magnitude error below $0.25\,\mathrm{dB}$ (cf. Fig. 4 in [18]). The resulting phase deviation is in this case below $1°$.

The low-pass and high-pass filters are realized as first-order passive filters with the components connected between the LF and HF signal buffers/amplifiers, which inherently sets the corner frequency of the two filters to the same value, regardless of component tolerances. This mitigates a further source of magnitude and phase deviation. To increase immunity against CM disturbances, e.g., from nearby switching actions, the combiner circuit is realized fully differentially and a simplified schematic is shown in **Fig. 3 (a)**. The finalized hardware prototype of the combiner circuit is shown in **Fig. 3 (b)**. Apart from the bulky connectors required for testing purposes, a very compact realization is possible with dimensions of only $25\,\mathrm{mm} \times 22\,\mathrm{mm}$. The final design includes PCB mounted shields for improved immunity against external disturbances, for example magnetic fields emerging from the loop formed by the connection of the main current to the Hall sensor.

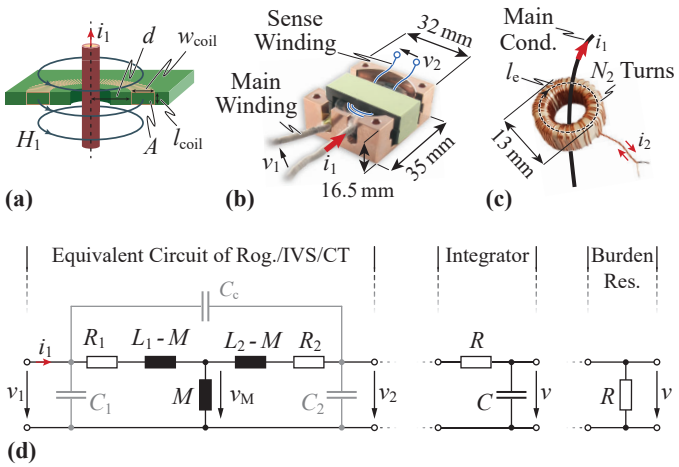

Fig. 4. HF Measurement sensors considered in [18]. **(a)** PCB-integrated circular Rogowski coil, **(b)** galvanically isolated inductor voltage sensing (IVS) realized on the existing output filter inductor and **(c)** current transformer (CT) realized on a small iron powder toroidal core. **(d)** General equivalent circuit with a passive integrator to terminate the Rogowski coil and/or the IVS or a low ohmic burden resistor to terminate the CT.

B. HF Measurement Sensors

The Hall sensor with the highest specified BW, i.e., $f_{\mathrm{Hall}} > 1\,\mathrm{MHz}$ [4], is chosen as a starting point in [18]. Three concepts to extend the BW of this LF sensor are investigated: 1) the conventional circular Rogowski coil, 2) the galvanically isolated inductor voltage sensing (IVS) and 3) the current transformer (CT). The three solutions are shown in **Fig. 4** including a general equivalent circuit and the required termination circuits.

1) Conventional Rogowski Coil: Rogowski coils generate a voltage v_2 that is proportional to the change in primary current ($\mathrm{d}i_1/\mathrm{d}t$), where the proportionality factor is the mutual inductance M. To get a signal proportional to the primary current i_1 the coil is loaded with a high impedance integrator, here realized with a passive RC network, with corner frequency $f_{\mathrm{int}} = 1/(2\pi \cdot RC)$. The coil is either realized as helical winding wrapped around the conductor to be measured or as PCB integrated solution. The latter is illustrated in **Fig. 4 (a)**. Due to the absence of a magnetic core, the sensor behaves very linear but has a low mutual inductance M (in the order of tens of nH). Its measurement sensitivity is directly proportional to M and the integrator corner frequency f_{int}. The latter is equal to the HF sensor's corner frequency $f_{\mathrm{c,HF}}$. Using a combiner circuit as shown in **Fig. 3** with $f_{\mathrm{c,HF}} < f_{\mathrm{filt}}$, the low M and the low required $f_{\mathrm{c,HF}}$ lead to an extremely small measurement sensitivity and thus dispose the classical Rogowski unsuitable as a HF sensor. As will be shown later, there are alternative approaches to combine the LF and HF signal where Rogowski coils become feasible.

2) Galvanically Isolated Inductor Voltage Sensing: A considerably higher measurement sensitivity is achieved when the inductor voltage is measured with an additional sense winding composed of a small number of turns on an already present output filter inductor L_{br} as shown in **Fig. 4 (b)**. The sense winding is terminated with a high impedance integrator circuit with $f_{\mathrm{int}} = f_{\mathrm{c,HF}} = 350\,\mathrm{Hz}$. Due to the galvanic isolation this concept is denoted *galvanically isolated inductor voltage sensing* (IVS). The underlying principle is identical to a

This article has been accepted for publication in IEEE Transactions on Industry Applications. This is the author's version which has not been fully edited and content may change prior to final publication. Citation information: DOI 10.1109/TIA.2022.3164865

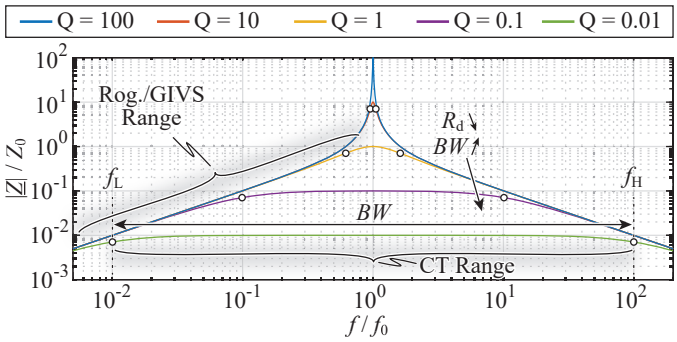

Fig. 5. Impedance of a Rogowski coil and/or IVS winding and/or CT secondary winding for different quality factors $Q = R_\mathrm{d}/Z_0$. For a given resonance frequency f_0 the peaking reduces with lower Q (lower R_d). Highlighted are the operation range of the Rogoswki coil and the IVS (range where Z increases with f) as well as the operation range of the CT (range where Z is constant).

Rogowski coil but thanks to the magnetic core with its relative permeability μ_r a significantly higher mutual inductance M ($M \approx 2.1\,\mu\mathrm{H}$) and thus a higher measurement sensitivity is achieved. In other words, for a given measurement sensitivity a lower corner frequency $f_\mathrm{c,HF}$ can be chosen. Furthermore, no additional volume for a dedicated coil is required, since the sense winding is directly placed on the inductor. However, a variation of μ_r, e.g., due to temperature variations or the non-linear $B - H$ characteristic of the magnetic material directly influences the measurement sensitivity. In practice, the effect is relatively small, since the air gap in the inductor linearizes the effective permeability. Same as the conventional Rogowski coil the BW of the IVS is implicitly limited by the self-resonance frequency (SRF) of the coil or sense winding [19]. The SRF $f_0 = 17.2\,\mathrm{MHz}$ is determined by the parallel resonance between the self-inductance L_2 and the equivalent parasitic capacitance $C_\mathrm{p} = C_2 || \frac{C_\mathrm{c} C_1}{C_\mathrm{c}+C_1}$ of the sense winding (cf. **Fig. 4 (d)**). Above the typically very weakly damped SRF the coil behaves capacitively and therefore does not measure the current anymore. A damping resistor R_d is often connected in parallel to the output of conventional Rogowski coils to damp the SRF, i.e., to flatten the peak. This prevents oscillations in the output signal in case the SRF is excited during operation. **Fig. 5** shows the effect of the added damping resistor R_d that effectively lowers the quality factor $Q = R_\mathrm{d}/Z_0$ of the coil. For $Q = 1/2$, i.e., $R_\mathrm{d} = Z_0/2 = 1/2 \cdot \sqrt{L_2/C_\mathrm{p}}$ there is no peaking (critical damping). For the IVS, thanks to the high coupling, several hundred volts appear at the sense winding. Therefore, damping is not practically possible in this case because the required R_d is usually in the few hundred ohm range, which would cause significant losses.

3) Current Transformer: A current transformer (CT) typically features one single primary turn N_1 and a high number of secondary turns N_2. **Fig. 4 (c)** shows a realization with $N_2 = 50$ turns on a small iron powder toroidal core. The high turns ratio allows the CT to be loaded with a small burden resistance R, which inherently damps the SRF by lowering Q to very small values without contributing high losses. From **Fig. 5** follows that the impedance is flat over a very wide frequency region for a low Q. Consequently, the CT requires no integration stage, since the output voltage v is directly proportional to the primary current i_1. The CT has to be able to carry the full DC current without saturation, thus a low-μ iron powder toroidal core is chosen (Micrometals T50-70B with a $\mu_\mathrm{r} = 100$). It's magnetic length l_e is selected such that the maximum expected current of $65\,\mathrm{A}$ leads to a decrease of the initial permeability by $< 25\,\%$. The corner frequency $f_\mathrm{c,HF}$ of the CT is determined by the self inductance L_2, the winding resistance R_2 and the burden resistance R and is selected $f_\mathrm{c,HF} = 1\,\mathrm{kHz}$ in the presented realization. It has to be emphasized, that the material non-linearities do influence L_2, which has no impact on the measurement sensitivity but only on the corner frequency $f_\mathrm{c,HF}$. If $f_\mathrm{c,HF}$ is sufficiently lower than f_filt, then the possible fluctuation of $f_\mathrm{c,HF}$ due to changes in μ_r do not alter the flatness of the overall transfer function (TF).

C. Experimental Verification

The IVS and the CT have been realized as hardware prototypes to experimentally verify the performance. TF measurements in the frequency domain and converter waveform measurements in the time domain reveal satisfactory performance. A BW of $10\,\mathrm{MHz}$ for the IVS and $35\,\mathrm{MHz}$ for the CT are achieved. Furthermore, a $1.6\,\mathrm{MHz}$ triangular current ripple could be accurately followed as a comparison with a reference measurement using a commercial current probe revealed. For detailed measurement results please refer to **Section V**.

III. Alternative Measurement System and Combiner Circuit

The advantage of the sensor combination presented in [18] is the inherently matched combiner low-pass and high-pass filter, independent of filter element component tolerances. This property comes at the expense of a large required overlap of the LF Hall-effect sensor and the HF current sensor in the frequency response (approximately three decades). Clearly, this is not optimal in terms of form factor and/or sensitivity of the individual sensors, particularly for a Rogowski coil, whose sensitivity is inversely proportional to its lower corner frequency for a given mutual inductance M. Therefore, alternative approaches of the combination without the required overlap have been proposed, e.g., in [7], [9], [12] and [14]. [7] and [9] present a gapped CT with a Hall element placed inside the air gap. This arrangement allows a combination of LF and HF signals without any processing electronics but requires custom magnetic components and careful placement of the Hall element to avoid measurement errors due to the magnetic stray field in the vicinity of the air gap.

The aim of this work is to realize an optimized high-bandwidth current sensor based on the concept of [12] and [14], which will be explained in the following, and compare the results with the findings of [18]. A major advantage thereby is that for a given measurement sensitivity compact Rogowski coils with a much lower mutual inductance can be used.

A. General Operation

Fig. 6 shows the block diagram of the alternative realization of the measurement system and combiner circuit as shown in [12] and [14]. The LF path is composed of the commercial fully integrated Hall-effect sensor with sensitivity $G_\mathrm{0,Hall}$ that shows a low-pass characteristic approximated with corner

This article has been accepted for publication in IEEE Transactions on Industry Applications. This is the author's version which has not been fully edited and content may change prior to final publication. Citation information: DOI 10.1109/TIA.2022.3164865

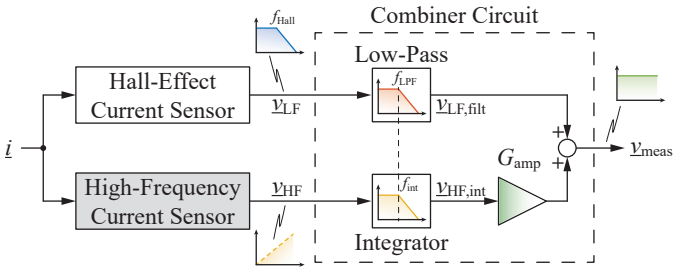

Fig. 6. Block diagram of the alternative current measurement system without the need for a large overlap between the LF and HF sensors. The HF sensor is assumed to react to the change in current ($\mathrm{d}i/\mathrm{d}t$), i.e., shows a differentiating behavior.

frequency f_{Hall}, and an additional low-pass filter (LPF) with corner frequency f_{LPF} sufficiently lower than f_{Hall}. The condition $f_{\mathrm{LPF}} \ll f_{\mathrm{Hall}}$ (at least one decade lower [7]) ensures that the filtered Hall sensor signal $\underline{v}_{\mathrm{LF,filt}}$ behaves like a first-order low-pass response despite the typically very complex frequency response of the Hall sensor itself [4]. The HF path consists of a HF sensor with a high-pass characteristic and an amplifier with gain G_{amp} (assumed constant over frequency and without phase-shift as explained later). The HF sensor is in this case assumed to react proportional to a change in current ($\mathrm{d}i/\mathrm{d}t$), i.e., $\underline{v}_{\mathrm{HF}} = sM \cdot \underline{i}$ in frequency domain. Thus, a subsequent integration stage realized as first-order *RC* low-pass filter with corner frequency f_{int} introduces a high-pass characteristic for the HF sensor and results in a signal $\underline{v}_{\mathrm{HF,int}}$ proportional to the current $\underline{i}$ above f_{int}. In frequency domain, the output voltage $\underline{v}_{\mathrm{meas}}$ of the measurement system is

$$\underline{v}_{\mathrm{meas}} = \underbrace{\underline{v}_{\mathrm{LF}} \cdot \frac{1}{1+s/\omega_{\mathrm{LPF}}}}_{\underline{v}_{\mathrm{LF,filt}}} + G_{\mathrm{amp}} \cdot \underbrace{\underline{v}_{\mathrm{HF}} \cdot \frac{1}{1+s/\omega_{\mathrm{int}}}}_{\underline{v}_{\mathrm{HF,int}}} \tag{2}$$

with $\omega = 2\pi \cdot f$. Substitution of the LF and HF sensor TF results in a total TF $\underline{G}_{\mathrm{tot}} = \underline{v}_{\mathrm{meas}}/\underline{i}$ of

$$\underline{G}_{\mathrm{tot}} = \underline{v}_{\mathrm{meas}}/\underline{i} = \underbrace{G_{0,\mathrm{Hall}} \cdot \frac{1}{1+s/\omega_{\mathrm{Hall}}}}_{\underline{G}_{\mathrm{Hall}}} \cdot \underbrace{\frac{1}{1+s/\omega_{\mathrm{LPF}}}}_{\underline{G}_{\mathrm{LPF}}} + G_{\mathrm{amp}} \cdot \underbrace{sM \cdot \frac{1}{1+s/\omega_{\mathrm{int}}}}_{\underline{G}_{\mathrm{HF-Sensor,int}}}. \tag{3}$$

Assuming $f_{\mathrm{Hall}} \gg f_{\mathrm{LPF}}$, (3) simplifies to

$$\underline{G}_{\mathrm{tot}} = G_{0,\mathrm{Hall}} \cdot \frac{1}{1+s/\omega_{\mathrm{LPF}}} + \underbrace{G_{\mathrm{amp}} \cdot M \cdot \omega_{\mathrm{int}}}_{\equiv G_{0,\mathrm{HF}}} \cdot \frac{s/\omega_{\mathrm{int}}}{1+s/\omega_{\mathrm{int}}}. \tag{4}$$

Two conditions have to be fulfilled for a flat $\underline{G}_{\mathrm{tot}}$:

i) The sensitivities of the Hall sensor and the HF sensor have to be matched, i.e., $G_{0,\mathrm{Hall}} = G_{\mathrm{amp}} \cdot M \cdot \omega_{\mathrm{int}}$.

ii) The LPF in the LF path and the integrator in the HF path must be set to the same corner frequency, i.e., $f_{\mathrm{LPF}} = f_{\mathrm{int}}$.

With i) and ii), (4) simplifies to

$$\underline{G}_{\mathrm{tot}} = G_{0,\mathrm{Hall}} \cdot \left(\frac{s/\omega_{\mathrm{LPF}}}{1+s/\omega_{\mathrm{LPF}}} + \frac{1}{1+s/\omega_{\mathrm{LPF}}} \right) = G_{0,\mathrm{Hall}}, \tag{5}$$

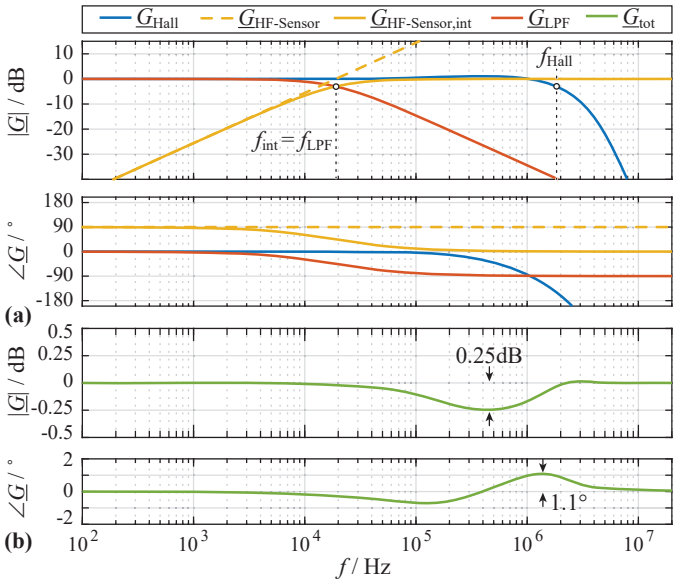

Fig. 7. Exemplary transfer functions (TFs) for the alternative combiner circuit with **(a)** normalized magnitude and phase response of the LF Hall sensor ($\underline{G}_{\mathrm{Hall}}$, taken from the datasheet [4]) with $f_{\mathrm{Hall}} \approx 1.8\,\mathrm{MHz}$, a HF current sensor ($\underline{G}_{\mathrm{HF-Sensor}}$) with $f_{\mathrm{c,HF}} = f_{\mathrm{int}} = 19\,\mathrm{kHz}$ and the accordingly matched low-pass filter ($\underline{G}_{\mathrm{LPF}}$). **(b)** Resulting normalized total TF $\underline{G}_{\mathrm{tot}}$ with a maximum magnitude and phase deviation of $0.25\,\mathrm{dB}$ and $1.1°$, respectively.

which is the summation of a low-pass and high-pass response with the same corner frequency $f_{\mathrm{LPF}} = f_{\mathrm{int}}$. $\underline{G}_{\mathrm{tot}}$ is thus constant over the full frequency range, limited in bandwidth only by the HF sensor itself. In contrast to the combiner circuit in [18], the HF sensor corner frequency f_{int} is identical to the combiner frequency (denoted f_{filt} in [18]), i.e., the frequency of the transition from LF to HF sensor. For a given required measurement sensitivity the HF sensor corner frequency can be chosen approximately two decades higher compared to [18] (in the range of tens of kHz instead of hundreds of Hz), which allows to use Rogowski coils with a mutual inductance approximately 100 times lower than the $M \approx 2\,\mu\mathrm{H}$ of the IVS. This will be further elaborated in **Section IV**.

Fig. 7 shows exemplary normalized TFs to illustrate the operation of the measurement system. Please note that the Hall sensor response $\underline{G}_{\mathrm{Hall}}$ is taken from the datasheet [4]. Despite the perfectly matched LF and HF sensor sensitivities and identical frequencies f_{LPF} and f_{int} ($f_{\mathrm{LPF}} = f_{\mathrm{int}} = 19\,\mathrm{kHz}$) in **Fig. 7 (a)**, the total TF $\underline{G}_{\mathrm{tot}}$ in **Fig. 7 (b)** shows an amplitude and phase mismatch of $0.25\,\mathrm{dB}$ and $1.1°$, respectively. This is due to the impact of the Hall sensor's frequency response on the LPF, resulting in a deviation of the behavior of $v_{\mathrm{LF,filt}}$ from an ideal first-order system.

B. Impact of Non-Idealities

1) Selection of the Combiner Frequency: The selection of f_{LPF} and thus the combiner frequency is the remaining degree of freedom in the LF path for the given Hall sensor frequency response. **Fig. 8 (a)** indicates the maximum magnitude deviation $\Delta|\underline{G}_{\mathrm{tot}}|$ of the total TF based on the selection of f_{LPF} under the assumption of ideal matching ($f_{\mathrm{LPF}} = f_{\mathrm{int}}$). Similarly, **Fig. 8 (b)** shows the maximum phase deviation $\angle\underline{G}_{\mathrm{tot}}$. It is intuitively clear that a lower f_{LPF} results in a smaller magnitude and phase deviation, since the overall

This article has been accepted for publication in IEEE Transactions on Industry Applications. This is the author's version which has not been fully edited and content may change prior to final publication. Citation information: DOI 10.1109/TIA.2022.3164865

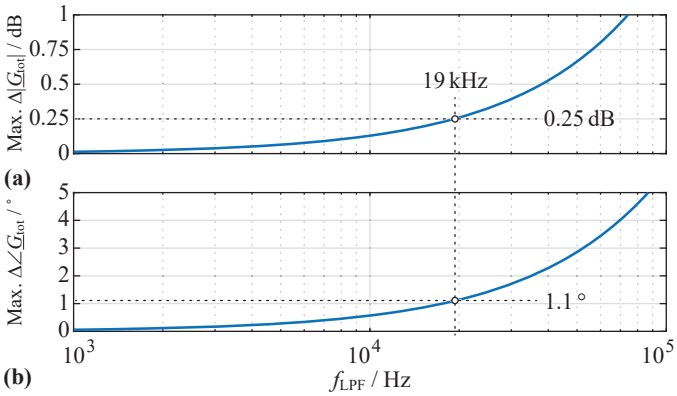

Fig. 8. Maximum magnitude deviation $\Delta|\underline{G}_{\mathrm{tot}}|$ and maximum phase deviation $\Delta\angle\underline{G}_{\mathrm{tot}}$ of the total TF $\underline{G}_{\mathrm{tot}}$ for different LPF corner frequencies f_{LPF}. Perfect matching, i.e., $f_{\mathrm{LPF}} = f_{\mathrm{int}}$ is assumed.

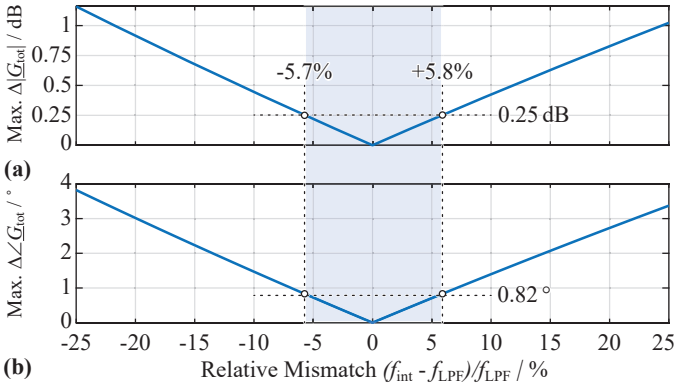

Fig. 9. Impact of a relative mismatch of f_{int} with respect to f_{LPF} on the maximum magnitude deviation $\Delta|\underline{G}_{\mathrm{tot}}|$ and maximum phase deviation $\Delta\angle\underline{G}_{\mathrm{tot}}$ of the total TF $\underline{G}_{\mathrm{tot}}$.

behavior is more accurately determined solely by the LPF and is not influenced by the Hall sensor's frequency response ($f_{\mathrm{LPF}} \ll f_{\mathrm{Hall}}$). As already shown, for $\Delta|\underline{G}_{\mathrm{tot}}| < 0.25\,\mathrm{dB}$ (around $3\,\%$ error), $f_{\mathrm{LPF}} < 19\,\mathrm{kHz}$ must be chosen. At the same time this implies $\angle\underline{G}_{\mathrm{tot}} < 1.1°$ (cf. **Fig. 7**).

2) Mismatch Between LF and HF Path: A mismatch between f_{int} and f_{LPF} violates condition ii) mentioned above and results in a deviation from the ideally flat behavior in the magnitude and phase response. **Fig. 9** depicts the maximum magnitude and phase deviation for a relative mismatch between f_{int} and f_{LPF}. In order to keep $\Delta|\underline{G}_{\mathrm{tot}}| < 0.25\,\mathrm{dB}$ the mismatch between the two corner frequencies needs to be lower than $-5.7/+5.8\,\%$. At the same time this results in a $\Delta\angle\underline{G}_{\mathrm{tot}}$ of $0.82°$. Both corner frequencies are realized with passive *RC* networks, and tolerances $< 5\,\%$ are easily achieved with readily available components. Manual trimming of the filter elements could improve this even further. Hence, the influence of component tolerances on the flatness of $\underline{G}_{\mathrm{tot}}$ is negligible.

A mismatch between the LF and HF sensor sensitivity (condition i) from above) similarly leads to a magnitude and phase deviation. To keep $\Delta|\underline{G}_{\mathrm{tot}}|$ below $0.25\,\mathrm{dB}$ the mismatch must be smaller than $\pm 3\,\%$. Adjustment of the amplifier gain G_{amp} allows to precisely match the sensitivities and therefore, this error contribution is negligible.

Remark: Instead of a sensor that reacts proportional to a current change $\mathrm{d}i/\mathrm{d}t$ and a subsequent integration stage, the HF current measurement could alternatively be realized with a CT as shown in [7], [9] and [18]. In this case, $f_{\mathrm{c,HF}}$ is determined by L_2, R_2 and R (cf. (5) in [18] and **Fig. 4**). For a variation of the flux density in the CT, the relative permeability μ_{r} changes based on the non-linear B-H characteristic. Similarly, temperature variations influence μ_{r}. Consequently, L_2 and therefore $f_{\mathrm{c,HF}}$ are not necessarily constant during operation, which violates the matching of the LF and HF sensor corner frequencies. Therefore, it is advisable to use a HF sensor with a subsequent passive RC integrator stage, to prevent a variation of $f_{\mathrm{c,HF}}$.

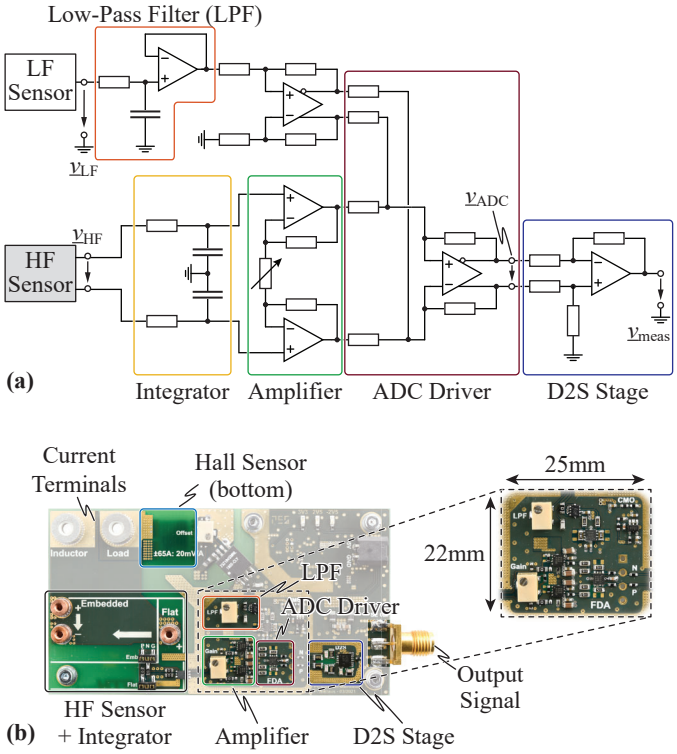

Fig. 10. (a) Simplified schematic of the fully differential combiner circuit and **(b)** picture of the realized hardware prototype for the performance verifications. Relevant circuit blocks are highlighted.

C. Practical Realization

A simplified circuit diagram of the combiner circuit is presented in **Fig. 10 (a)** together with a picture of the realized hardware prototype in **Fig. 10 (b)**. All the relevant building blocks are highlighted. The circuit is realized fully differentially to improve the robustness against CM disturbances. Both, the differentially implemented integrator (yellow) as well as the LPF after the Hall sensor (orange) are realized as passive *RC* circuits. After the HF sensor amplifier stage (green) with adjustable gain the signals are summed up and the ADC driver (dark red) is the interface to a high-speed fully differential ADC. For the performance verification, however, a single-ended output signal is required (cf. **Section V**). Therefore, the final stage is a high CM Rejection Ratio (CMRR) differential to single-ended (D2S) conversion (dark blue). The circuit from **Fig. 10 (a)** without the D2S conversion is realized extremely compact with an area of only $22 \times 25\,\mathrm{mm}$. The hardware prototype further includes connectors to mount different HF sensors (cf. **Section IV**).

IV. PCB Integrated Pickup Coils

A. HF Sensor Sensitivity

The alternative combiner circuit from the previous section requires a significantly smaller overlap between the LF and HF sensor. Consequently, for a given Hall sensor bandwidth, a HF sensor with higher corner frequency f_{int} can be used. In case of a conventional Rogowski coil (cf. **Fig. 4 (a)**) the required mutual inductance M can be calculated based on f_{int} and the required sensor sensitivity. Assuming an ADC full-scale range of 2 V peak-to-peak and a maximum current measurement range of ± 65 A, the measurement sensitivity is 15.4 mV/A. The HF sensor's sensitivity $G_{0,\mathrm{HF}}$ is increased with G_{amp}, which is typically constrained to values below 10, due to the finite gain-bandwidth product. As a conservative estimate $G_{\mathrm{amp}} = 5$ is assumed in the following, which gives a large-signal (2 V peak-to-peak) bandwidth of around 200 MHz with a typical high-speed operational amplifier [20]. Therefore, the amplifier's frequency response can be neglected for the considered measurement frequency range (G_{amp} in (2) is constant over frequency and has no phase-shift). According to (4), the HF sensor's sensitivity is

$$G_{0,\mathrm{HF}} = G_{\mathrm{amp}} \cdot M \cdot \omega_{\mathrm{int}} = G_{\mathrm{amp}} \cdot \frac{M}{RC}, \qquad (6)$$

where $\omega_{\mathrm{int}} = 1/(RC)$ is the *RC*-integrator corner frequency (cf. **Fig. 6**). While the combiner circuit in **Section II** requires $f_{\mathrm{int}} < 500$ Hz for $\Delta|\underline{G}_{\mathrm{tot}}| < 0.25$ dB, with the alternative approach $f_{\mathrm{int}} < 19$ kHz is sufficient. Therefore, the required mutual inductance M for $G_{0,\mathrm{HF}} = 15.4$ mV/A is only 25.8 nH for the combiner circuit according to **Section III**. That is almost 100 times lower compared to the $M \approx 2\,\mu$H in case of the IVS with a circuit according to **Section II**. A mutual inductance in the tens of nH range is feasible with Rogowski coils with the added benefit of high linearity due to the absence of a magnetic core material (no saturation, no material dependent M, etc.). A PCB integrated realization is beneficial not only in terms of accurate, economical and reproducible manufacturing but also in terms of tighter controlled parasitic elements.

B. Investigated Coil Geometries

PCB integrated Rogowski coils have been comprehensively studied in literature. Within this work we differentiate between the conventional circular Rogowski coil geometry shown in **Fig. 11 (a)** and several improved arrangements in **Fig. 11 (b)-(d)**, which we hereinafter denote as *pickup coils* (PUCs). The investigated PUC geometries are based on previously studied designs in the literature [21]–[25]. Those are, however, mainly focusing on switch current measurements in power semiconductors during the typically very fast switching transitions for characterization, diagnostic and protection purposes, and therefore have a rather low M. Furthermore, no DC and LF component is provided, which, however, is mandatory for current control in converter systems. In this work we investigate the conventional Rogowski coil geometry as well as three improved PUC arrangements for suitability as HF BW extension for a Hall-effect current sensor. Thereby, not only a small form factor but also a large enough $M \approx 25$ nH and a low variation of M versus frequency is important.

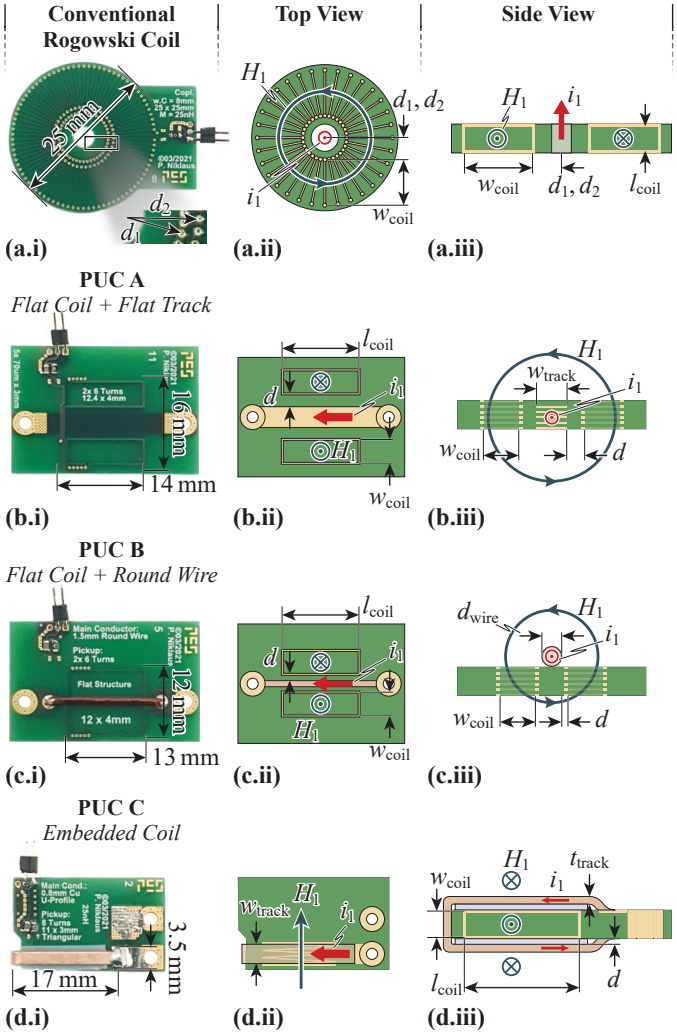

Fig. 11. Investigated pickup coil (PUC) geometries. **(a.i)** Picture of the conventional circular Rogowski coil with **(a.ii)** schematic top and **(a.iii)** side view with indicated directions of the main current i_1 and the magnetic field H_1 as well as the coil dimensions. **(b)**, **(c)** and **(d)** show the same for PUC arrangements A, B and C, respectively.

The geometry for each PUC arrangement is selected with a design procedure that considers the following performance criteria:

i) nominal mutual inductance of $M = 25$ nH,
ii) minimum variation of M versus frequency,
iii) maximum bandwidth,
iv) minimum occupied area.

Table I summarizes the properties of the four investigated geometries as a result of the detailed analysis in the following paragraphs. $\mathrm{d}M_{\mathrm{f}}$ denotes the relative variation of M in the frequency range $f \in [20\,\mathrm{kHz} \ldots 20\,\mathrm{MHz}]$ with respect to M at $f = 20$ kHz ($\approx f_{\mathrm{int}}$) and is defined as

$$\mathrm{d}M_{\mathrm{f}} = \frac{\max\{M(f)\} - \min\{M(f)\}}{M(f = 20\,\mathrm{kHz})} \cdot 100\,\%. \qquad (7)$$

1) Conventional Rogowski Coil:
The conventional PCB integrated Rogowski coil geometry directly follows from the helical coil wrapped around a conductor. The main current carrying conductor is inserted in the center of the circular PCB (cf. **Fig. 11 (a)**) with a radially symmetrically arranged coil of width w_{coil} and length l_{coil}. For

a distance d between the center of the main current conductor and the inner edge of the coil, the mutual inductance M of a coil with N turns is found as [16]

$$M = \frac{\mu_0 \cdot N \cdot l_{\mathrm{coil}}}{2\pi} \cdot \ln\left(1 + \frac{w_{\mathrm{coil}}}{d}\right). \tag{8}$$

M scales proportionally with N and l_{coil} but only logarithmically with increasing w_{coil} because the magnetic field decreases with $1/r$ in radial direction r. Unfortunately, w_{coil} and N are the only design parameters to choose, since l_{coil} is limited by the PCB thickness to around $1.5\,\mathrm{mm}$. Clearly, increasing w_{coil} only marginally increases M given the logarithmic scaling. The self-inductance L_2 (cf. equivalent circuit in **Fig. 4 (d)**), which together with C_{p} defines the coil's SRF and ultimately its bandwidth (cf. **Fig. 5**) [19], however, scales linearly with w_{coil}. The number of turns is limited by the maximum number of vias that can be placed on the inner edge of the coil (distance d from the center) while meeting the PCB manufacturing process clearances. On the one hand, d should be kept low to increase M but on the other hand the maximum N is a function of d. While M scales linearly with N, L_2 scales quadratically and thus the ratio M/L_2, which is a measure for the coupling coefficient, decreases with $1/N$. To achieve a certain M, comparably large coils with a high N are required, which is detrimental for the SRF and for the coupling coefficient.

With a second layer of vias on the inner edge of the coil, N and thus M can be increased. Under the assumption that $N/2$ of the turns are formed with the first layer of vias on the inner coil edge (distance d_1 from the center, cf. **Fig. 11 (a.i)**) and the remaining $N/2$ turns with the second layer of vias (distance d_2 from the center, cf. **Fig. 11 (a.i)**), the mutual inductance is analytically calculated as

$$M = \frac{N}{2} \cdot \frac{\mu_0 \cdot l_{\mathrm{coil}}}{2\pi} \cdot \ln\left(\frac{(d_1 + w_{\mathrm{coil}})^2}{d_1 \cdot d_2}\right) \tag{9}$$

based on (8). The coil geometry with minimal occupied area (overall diameter of $25\,\mathrm{mm}$) is found by iterating through all possible geometries that achieve the required $M = 25\,\mathrm{nH}$ using (9). The resulting coil occupies an area of $490\,\mathrm{mm}^2$ and features $N = 86$ turns (cf. **Table I**).

2) Pickup Coil A - Flat Coil + Flat Conductor:
Compared to the conventional geometry the coupling and hence the mutual inductance can be improved if the coil is in parallel to the main conductor, since M scales proportionally with the coil length. **Fig. 11 (b)** shows a picture and top and side view of such an arrangement where the main conductor is realized directly on the PCB with tracks of width w_{track} on multiple layers (5 of totally 6 layers in this case). In fact, the side view of the conventional Rogowski coil now becomes the top view with l_{coil} and w_{coil} as design parameters. This arrangement is based on realizations shown [21], [22] and [23]. The N turns of the PUC are not anymore symmetrically placed around the main track but lie equally distributed on the left and right side of the main conductor in the same plane ($N/2$ on each side). In the following, this arrangement is called *PUC A*. Compared to the simple case of the conventional Rogowski coil, analytical formulas are not easily derived due to the rectangular cross section of the main conductor distributed among multiple layers. In addition, HF effects such as the skin and proximity effect lead to an inhomogeneous current distribution within the main conductor at elevated frequencies with a significant increase of the current density on the outer edges. This results in a large $\mathrm{d}M_{\mathrm{f}}$ as indicated in **Table I**. This effect is particularly detrimental for wide tracks compared to their thickness. At the same time, w_{track} has to be several millimeters wide to constrain the DC current density to values in the range of $40\,\mathrm{A/mm}^2$ for sufficient heat extraction (empirical value).

TABLE I. Parameters of the four selected geometries of the investigated Rogowski coil/PUC arrangements for a nominal $M = 25\,\mathrm{nH}$ resulting from 2D FEM simulations and the considered design process.

Sensor	N	w_{coil} mm	l_{coil} mm	d mm	$\frac{w_{\mathrm{track}}}{d_{\mathrm{wire}}}$ mm	Total Area mm^2	$\mathrm{d}M_{\mathrm{f}}$ %
Rogowski	86	8.0	1.5	4.2 (d_1) 5.1 (d_2)	n.a.	490	0.1
PUC A	12	4.0	12.4	1.2	3.3	224	3.9
PUC B	12	4.0	12.0	0.25	1.25	156	0.0
PUC C	8	1.5	11.8	0.4	2.5	60	0.9

The magnetic field distribution is obtained for different frequencies up to $20\,\mathrm{MHz}$ with help of a 2D finite element method (FEM) simulation for different w_{track}. With the known magnetic field distribution the remaining parameters of the coil, namely the distance d between main track and coil edge, the coil width w_{coil} and the coil length l_{coil} could be varied in post processing to select a suitable geometry for the given performance criteria. At the same time, side conditions such as maximum current density (thermal limit) and minimum isolation distances (safety limit) have to be considered. The latter condition implies a lower bound of $1.2\,\mathrm{mm}$ for d. Please note that for the utilized 6-layer PCB the number of turns is always fixed to $N = 2 \cdot 6 = 12$ under the assumption of one winding per layer. The parameters of the selected geometry of PUC A are listed in **Table I**. As expected, the frequency variation $\mathrm{d}M_{\mathrm{f}}$ is rather large, however the required total area of $224\,\mathrm{mm}^2$ is more than halved compared to the conventional Rogowski coil. Please note that the parameters refer to the physical realization of the coil, where $l_{\mathrm{coil}} = 12.4\,\mathrm{mm}$ is selected slightly higher than the strictly required value of $10\,\mathrm{mm}$ for $M = 25\,\mathrm{nH}$. Generally, M is linearly dependent on l_{coil}, hence a variation of l_{coil} has no impact on $\mathrm{d}M_{\mathrm{f}}$.

3) Pickup Coil B - Flat Coil + Round Conductor:
The variation of M versus frequency is virtually eliminated if the main conductor from PUC A is replaced with a solid round wire (diameter d_{wire}) that is soldered directly on the PCB like a through hole component. This arrangement is denoted as *PUC B* and is depicted in **Fig. 11 (c)**. Further advantages are that the copper cross section compared to its diameter is much higher than it is on a PCB track and in addition, d can be reduced, provided the round wire features adequate isolation, e.g., enameled copper wire. The coil dimensions are found with the same design procedure described for PUC A. The parameters of the selected design are listed in **Table I**. Thanks to the much smaller d, the total area is only $156\,\mathrm{mm}^2$. Similar to PUC A, $l_{\mathrm{coil}} = 12.0\,\mathrm{mm}$ is chosen slightly larger than the strictly required value of $11.6\,\mathrm{mm}$ for $M = 25\,\mathrm{nH}$.

Remark: For PUC A and PUC B the rectangular turns are placed on the different PCB layers on top of each other as illustrated in **Fig. 11 (b.iii) and (c.iii)**. Measurements with modified arrangements where the turns on adjacent layers are offset by the track width to minimize the parasitic capacitance

showed a slight increase of the SRF, although the effect is minor.

4) Pickup Coil C - Embedded Coil:

An increased coupling is achieved with a coplanar arrangement (*PUC C*) as shown in **Fig. 11 (d)**. This arrangement has been shown in [23], [24] and [25]. Here, the coil is embedded between the main conductor, which is wrapped around the PCB. If the main current conductor should be realized on the same PCB, the small thickness of the copper foil (70 µm on a typical power PCB) implies wide tracks to meet the current density requirement. As already explained for PUC A, this results in a substantial variation of M over frequency. Furthermore, an expensive PCB technology with buried vias would be needed to realize the embedded coil on the inner layers with the additional drawback of a smaller w_{coil} (cf. **Fig. 11 (d.iii)**). Therefore, it is advisable to use an external copper bar of thickness $t_{\mathrm{track}} > 70\mu\mathrm{m}$ to simultaneously lower w_{track}. The coplanar arrangement has several distinct advantages:

i) The magnetic field sensed by the coil is doubled compared to a single track, since the current passes around the coil on both sides with opposite sign.
ii) The current distribution along the width of the tracks is more uniform compared to a single track, hence the frequency dependence of M is lower (but not eliminated).
iii) As mentioned in [24], the copper bar additionally shields the coil from external magnetic fields.
iv) The sensor can be very easily connected in power electronic systems because the main current terminals lie next to each other.

A disadvantage is the somewhat higher parasitic coupling capacitance C_{c} between main current track and coil.

A suitable geometry for PUC C is found based on the magnetic field distribution simulated with 2D FEM using the same procedure as for PUC A and PUC B. The number of turns N is now an additional degree of freedom, since the turns are formed with tracks on the top and bottom layer connected with vias. The isolation between PUC and main conductor is realized with a PTFE foil of thickness $d = 0.4\,\mathrm{mm}$. The value is selected based on a trade-off between parasitic coupling capacitance between PUC and main conductor, and the achievable mutual inductance. The copper bar thickness is selected as $t_{\mathrm{track}} = 0.5\,\mathrm{mm}$. The results in **Table I** reveal that with an area of only $60\,\mathrm{mm}^2$, PUC C is by far the smallest realization (area reduction by a factor of 8 compared to the conventional Rogowski coil), while the $\mathrm{d}M_{\mathrm{f}}$ is below $1\,\%$.

C. Mutual Inductance and Coil Impedance

The conventional Rogowski coil and the three PUCs are built based on the results listed in **Table I**. To verify the value of the mutual inductance at different frequencies, a current is injected in the main conductor while simultaneously the output voltage of the coil is measured. It has to be ensured that the loop of the injected current is large enough, such that the measurement is not influenced by additional magnetic field components, e.g., from the return conductor. **Table II** summarizes the measurements at $f = \{100\,\mathrm{kHz}, 1\,\mathrm{MHz}, 5\,\mathrm{MHz}\}$ and compares them with the results from the FEM simulation.

There, the relative error ε_{M} between the simulated and measured value of M is defined as

$$\varepsilon_{\mathrm{M}} = (M_{\mathrm{meas}} - M_{\mathrm{FEM}})/M_{\mathrm{FEM}} \cdot 100\,\%. \qquad (10)$$

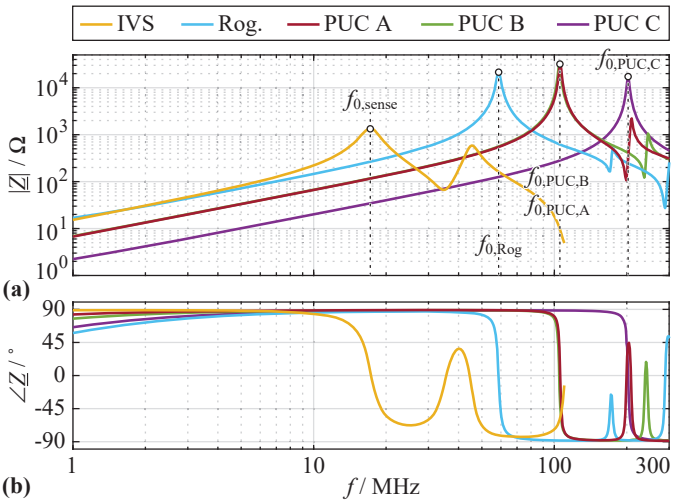

Fig. 12. Impedance measurements of the investigated PUCs as well as the IVS. **(a)** Magnitude and **(b)** phase response with highlighted self-resonance frequency (SRF) for each coil.

Generally, the measurement results agree very well with the FEM simulation with an error of less than $25\,\%$. The deviations can be explained with the slightly larger effective coil cross-sections in the hardware prototypes. The reason for this is the placement of the vias to connect the different layers as well as the return conductor from the last turn back to the first. The layout ensures that each turn has the minimum width and length of w_{coil} and l_{coil} as listed in **Table I**, respectively.

The parameter $\mathrm{d}M_{\mathrm{f}}$ could not be evaluated with this direct measurement method, since the additional capacitive loading of the coil voltage measurement drastically decreases the SRF to values around or even below $20\,\mathrm{MHz}$. The flatness of M vs. frequency will be discussed in **Section V-A**.

As illustrated in **Fig. 5** the BW of the HF sensors is limited to values below their SRF. Therefore, the impedance of the coils is measured with a precision impedance analyzer (Keysight E4991B [26]) to determine the SRF and the self-inductance L_2 of each prototype. **Fig. 12** shows the self-impedance measurements of the PUCs in comparison with the sense winding of the IVS described in **Section II** and **Table II** lists the numerical values for the SRF and L_2. Clearly, the conventional Rogowski coil has the highest $L_2 = 2.32\,\mu\mathrm{H}$ due to its high number of turns. PUC C has the lowest number of turns and the lowest area per turn ($w_{\mathrm{coil}} \cdot l_{\mathrm{coil}}$) and hence has the lowest $L_2 = 320\,\mathrm{nH}$. Additionally, numerical results for the coupling capacitance C_{c} between primary and secondary side are given. As expected, the coplanar arrangement (PUC C) has the highest C_{c}. Compared to the IVS with a SRF of around $f_{0,\mathrm{sense}} = 17\,\mathrm{MHz}$, an improvement up to a factor 12 is achieved with the PUCs. In alignment with L_2, the conventional Rogowski coil has the lowest SRF of $f_{0,\mathrm{Rog}} = 58\,\mathrm{MHz}$ whereas PUC C achieves the highest SRF of $f_{0,\mathrm{PUC,C}} = 202\,\mathrm{MHz}$. Given the similar dimensions and the similarity of their structures, PUC A and B have almost identical coil impedances and an SRF of $f_{0,\mathrm{PUC,A}} = f_{0,\mathrm{PUC,B}} = 105\,\mathrm{MHz}$. However, thanks to the smaller surface of the main track C_{c} is lower for PUC B. **Table II** further lists the ratio M/L_2, which is a measure for the magnetic coupling coefficient of each arrangement. A higher value thereby means, that the desired quantity M (related to the measurement sensitivity) is large compared to the undesired quantity L_2 (related to the SRF).

TABLE II. Simulated and measured mutual inductance of the four hardware prototypes including the results from the coil impedance measurements.

Sensor	M_{FEM} nH			M_{meas} nH			ε_{M} %			SRF MHz	L_2 µH	R_2 Ω	C_{c} pC	M/L_2
	100k	1M	5M	100k	1M	5M	100k	1M	5M					M @ 100 k
Rog.	25.0	25.0	25.0	23.8	23.2	25.2	-4.9	-7.2	0.8	58	2.32	8.6	1.0	0.010
PUC A	27.3	27.8	27.9	31.6	31.1	33.2	15.7	11.7	19.2	105	1.06	0.7	3.9	0.030
PUC B	30.1	30.1	30.1	36.1	35.2	37.1	19.7	16.9	23.2	105	1.07	1.3	2.3	0.034
PUC C	28.6	28.8	28.9	30.2	29.7	30.1	5.7	2.9	4.4	202	0.32	0.8	5.3	0.094

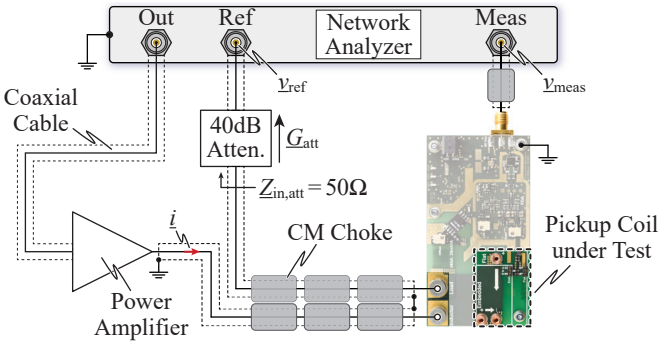

Fig. 13. Setup for the frequency response measurements.

For PUC C this ratio is almost a factor of 10 better compared to the conventional Rogowski coil, which results in a much higher SRF for the same sensitivity (better coupling).

V. Experimental Verification

The extension of the BW of a commercial Hall-effect current sensor by means of a PCB integrated Rogowski coil/PUC using the combiner circuit presented in **Section III** is experimentally verified in frequency and time domain. Furthermore, the results are compared with measurements using the IVS and the CT from [18] with the combiner circuit summarized in **Section II**. To maximize the bandwidth of the conventional Rogowski coil and the PUCs, the two integrator resistors R are placed directly at the coil terminals [19]. In this way, the additional capacitance of the connection to the combiner circuit does not lower the SRF.

A. Frequency Response

The small-signal frequency response is measured using a network analyzer (Omicron Lab Bode 100 [27]) with the setup shown in **Fig. 13**. A stimulus current $i = 1\,\mathrm{A}$ (peak-to-peak) is injected to the sensor under test with the help of a power amplifier to boost the network analyzer's output signal. The network analyzer determines the sensor TF by comparing the sensor output $\underline{v}_{\mathrm{meas}}$ with a reference measure $\underline{v}_{\mathrm{ref}}$ obtained with a precision $50\,\Omega$ 40 dB high-power radio-frequency (RF) attenuator (apitech/Weinschel 58-40-33 [28]). In fact, the RF attenuator behaves like a coaxial shunt, which provides a fixed load impedance of $50\,\Omega$ for the RF power amplifier. The measured TF $\underline{G}_{\mathrm{meas}}$ is then

$$\underline{G}_{\mathrm{meas}} = \frac{\underline{v}_{\mathrm{meas}}}{\underline{v}_{\mathrm{ref}}} = \frac{\underline{v}_{\mathrm{meas}}}{\underline{i} \cdot \underline{Z}_{\mathrm{in,att}} \cdot \underline{G}_{\mathrm{att}}} = \frac{\underline{G}_{\mathrm{tot}}}{\underline{Z}_{\mathrm{in,att}} \cdot \underline{G}_{\mathrm{att}}} \tag{11}$$

from which the total sensor TF $\underline{G}_{\mathrm{tot}} = \underline{v}_{\mathrm{meas}}/\underline{i}$ can be calculated if the attenuator's input impedance $\underline{Z}_{\mathrm{in,att}}$ and attenuation factor $\underline{G}_{\mathrm{att}}$ are known. All connections are made using coaxial cables with CM chokes placed around to prevent circulating ground currents at high frequencies.

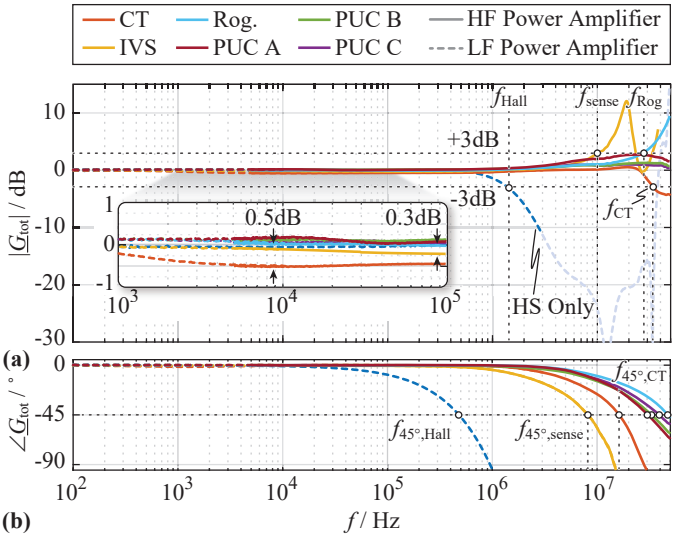

Fig. 14. Frequency response measurements of the Hall sensor alone (blue), the BW extension with IVS and CT investigated in [18] (yellow and red) and the conventional Rogowski coil + the proposed PUCs (cyan, dark red, green and purple). Measurements are performed with a LF power amplifier for the lower frequency range (dashed lines) and a HF power amplifier for the higher frequency range (continuous lines).

Fig. 14 shows the measured normalized TFs of the Hall sensor alone (blue), the Hall sensor extended with the CT (orange), the IVS (yellow), a conventional Rogowski coil (cyan), PUC A (dark red), PUC B (green) and PUC C (purple). A LF power amplifier for frequencies up to 3 MHz (dashed lines) and a HF power amplifier for frequencies between 5 kHz and 50 MHz (continuous lines) are used. **Table III** lists the exact configuration of the HF sensors and the achieved BW, where f_x denotes the $-3\,\mathrm{dB}$ point and $f_{45°,x}$ the frequency at which the phase is shifted by $-45°$. It has to be noted that the frequency response includes the phase-shift of the utilized cables and the RF attenuator, hence the displayed phase-shift is larger than the one of the current sensor alone. A manual correction is not performed here, since in a practical

TABLE III. Key performance parameters of the frequency response of all compared sensors. n.a. = not applicable.

Sensor	f_x	$f_{45°,x}$	f_{int}	f_{filt}
Hall only	1.4 MHz	490 kHz	n.a.	n.a.
Hall + Sense	10 MHz	8.2MHz	350 Hz	15.2 kHz
Hall + CT	35 MHz	16.5 MHz	1 kHz	24.5 kHz
Hall + Rog.	28 MHz	47 MHz	19 kHz	n.a.
Hall + PUC A	> 50 MHz	30.5 MHz	19 kHz	n.a.
Hall + PUC B	> 50 MHz	33 MHz	19 kHz	n.a.
Hall + PUC C	> 50 MHz	39 MHz	19 kHz	n.a.

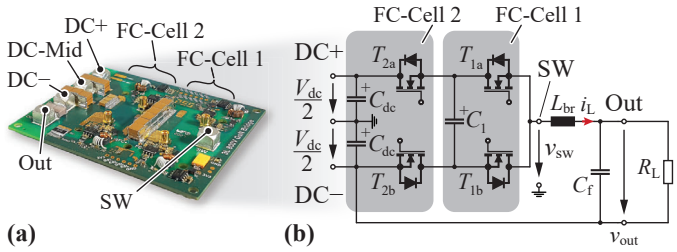

Fig. 15. **(a)** Hardware demonstrator of a single three-level branch of the GaN *3L3* AC power source and **(b)** the corresponding schematic diagram of the configuration for DC/DC operation with $V_{\mathrm{dc}} = 600\,\mathrm{V}$ (split DC-link) and an output load referred to the negative DC rail.

application this is usually not possible as well. Therefore, the f_{-45° values listed in **Table III** are conservative estimates.

Due to the low SRF, the conventional Rogowski coil as well as the IVS have the lowest BW, which is in accordance with the impedance measurements (cf. **Fig. 12**). The peaking due to the SRF is already visible in both cases, since no damping is provided. Hence, f_x in those cases denotes the frequency at which the amplitude is $+3\,\mathrm{dB}$ above the nominal value. The placement of a damping resistor R_{d} would reduce the peaking (cf **Fig. 5**) but would at the same time lead to a larger phase-shift already below the SRF. The PCB integrated PUCs achieve a significantly higher BW compared to the IVS and CT, in fact the $-3\,\mathrm{dB}$ point could not be identified with the available measurement equipment, that allows to measure up to $50\,\mathrm{MHz}$. The SRF measurements in **Fig. 12** indicate an even higher BW ($100 - 200\,\mathrm{MHz}$). This proves that the compact PUCs are a very convenient solution to extend the BW of an existing LF current sensor.

With help of frequency response measurements the sensitivities of the LF and HF path can be trimmed by manually adjusting the gain G_{amp} until the sensitivity at very low frequencies ($f \ll f_{\mathrm{c,HF}}$) equals the sensitivity at high frequencies ($f \gg f_{\mathrm{c,HF}}$). The flatness around the combiner frequency $f_{\mathrm{c,HF}}$ is improved by trimming the LPF. A zoomed view in **Fig. 14 (a)** reveals excellent flatness of the TF ($< 0.3\,\mathrm{dB}$, i.e., $< 3.5\,\%$ for all sensors except the CT). Therefore, the variation of M versus frequency in the PUCs ($\mathrm{d}M_{\mathrm{f}}$) is generally very low. It is, however, visible that PUC A in accordance with the calculations from **Table I** shows the highest $\mathrm{d}M_{\mathrm{f}}$.

B. Time-Domain Behavior

To verify the time-domain behavior, a hardware demonstrator of one three-level branch of the GaN *3L3* AC power source with $V_{\mathrm{dc}} = 600\,\mathrm{V}$ is used in DC/DC operation to generate a reference inductor current i_{L}. **Fig. 15 (a)** and **(b)** show a picture and the circuit of the hardware demonstrator, which is supplied with a split DC link $V_{\mathrm{dc}}/2 = 300\,\mathrm{V}$. The converter operates with a fixed duty-cycle of $D = 0.7$ and a switching frequency of $f_{\mathrm{sw}} = 800\,\mathrm{kHz}$. This results in a current ripple of $\approx 11.5\,\mathrm{A}$ peak-to-peak at $f_{\mathrm{iLpp}} = 1.6\,\mathrm{MHz}$. The load resistor R_{L} is chosen to ensure a strictly positive i_{L} to obtain one hard and one soft switching transition per effective switching period T_{iLpp}. **Fig. 16** depicts waveforms of the resulting switch-node voltage v_{sw} (cyan) and inductor current i_{L} over 2.5 effective switching periods. i_{L} is measured with a $120\,\mathrm{MHz}$ BW current probe [29] (green) and the Hall sensor extended with **(a)** the IVS, **(b)** the CT, **(c)** the conventional Rogowski coil, **(d)** PUC A, **(e)** PUC B and **(f)** PUC C (purple curves). Both, the proposed sensor and the current probe are placed after the output filter inductor L_{br}, i.e., at the converter output, to reduce the effect of fast voltage transients at the switch-node. Evidently, all sensor concepts accurately replicate the $1.6\,\mathrm{MHz}$ triangular current ripple. Therefore, the BW is in all cases enough to capture the relevant harmonic content. The conventional Rogowski coil and the PUCs are in this case critically damped with a damping resistor and therefore, even for the conventional Rogowski coil with the lowest SRF, no oscillations are visible. Please note that the asymmetry in the zero-voltage of v_{sw} arises from a slight deviation of the flying capacitor voltage from the ideal value of $V_{\mathrm{dc}}/2$.

It was verified in [18] that the Hall sensor alone is not enough to get an adequate representation of the inductor current as it shows a quasi-sinusoidal shape instead of a triangular one, too small amplitude and a large phase-shift compared to the current probe reference measurement.

VI. Common-Mode Rejection Ratio

To show the influence of CM disturbances occurring from fast switching transients ($\mathrm{d}v/\mathrm{d}t$) on the current sensor performance the measurements of **Fig. 16** are repeated in **Fig. 17**, this time with the current sensor placed *before* the output filter inductor, i.e., at the switch-node. Thereby, the current measurement is exposed to the full $\mathrm{d}v/\mathrm{d}t$ of $35 - 40\,\mathrm{kV/\mu s}$ at the switch-node. Additionally, the measurements with the sensor placed after the inductor are included in light color for easier comparison. The measurements with the PUCs show distinct error peaks during the switching transitions ($\approx 3\,\mathrm{A}$ for PUC A, $\approx 2\,\mathrm{A}$ for PUC B and $\approx 1.5\,\mathrm{A}$ for PUC C) as well as a small error during the rising and falling current slopes. The conventional Rogowski coil does not have distinct error peaks during the switching transitions but an increased error during the current slopes ($\approx 1\,\mathrm{A}$). The IVS and CT measurements remain almost unaffected.

To understand the impact of CM disturbances on the measured currents, **Fig. 18** shows a simplified CM equivalent circuit of the measurement system. The CM voltage v_{CM} from the switching transitions is represented with a CM voltage source. The coil is modeled with L_2, R_2 and C_2 based on the lumped element equivalent circuit (cf. **Fig. 4 (d)**). Additionally, the damping resistor R_{d} is included. The differential integrator giving the voltages $\underline{v}_{\mathrm{p}}$ and $\underline{v}_{\mathrm{n}}$ is formed with two *RC* low-pass filters (R_{p}, C_{p} and R_{n}, C_{n}), which are nominally identical. Given the fully differential realization a superior CMRR would be expected. However, four effects with a detrimental impact on the rejection of such CM disturbances are identified:

i) The CM impedance $\underline{Z}_{\mathrm{CM}}$ that determines the total CM current $\underline{i}_{\mathrm{CM}}$ for a given $\underline{v}_{\mathrm{CM}}$. A high $\underline{Z}_{\mathrm{CM}}$ results in a low $\underline{i}_{\mathrm{CM}}$ and therefore in lower distortions. Assuming a perfectly matched integrator, i.e., $R_{\mathrm{p}} = R_{\mathrm{n}} = R$ and $C_{\mathrm{p}} = C_{\mathrm{n}} = C$, $\underline{Z}_{\mathrm{CM}}$ is given by

$$\underline{Z}_{\mathrm{CM}} = \frac{s \cdot \frac{R}{2} \cdot \frac{C_{\mathrm{c}} \cdot 2C}{C_{\mathrm{c}} + 2C} + 1}{s \cdot \frac{C_{\mathrm{c}} \cdot 2C}{C_{\mathrm{c}} + 2C}} \overset{2C \gg C_{\mathrm{c}}}{\approx} \frac{R}{2} + \frac{1}{s \cdot C_{\mathrm{c}}}, \quad (12)$$

with the coupling capacitance C_{c} between primary and secondary side (cf. **Fig. 4**). The values of C_{c} for the

This article has been accepted for publication in IEEE Transactions on Industry Applications. This is the author's version which has not been fully edited and content may change prior to final publication. Citation information: DOI 10.1109/TIA.2022.3164865

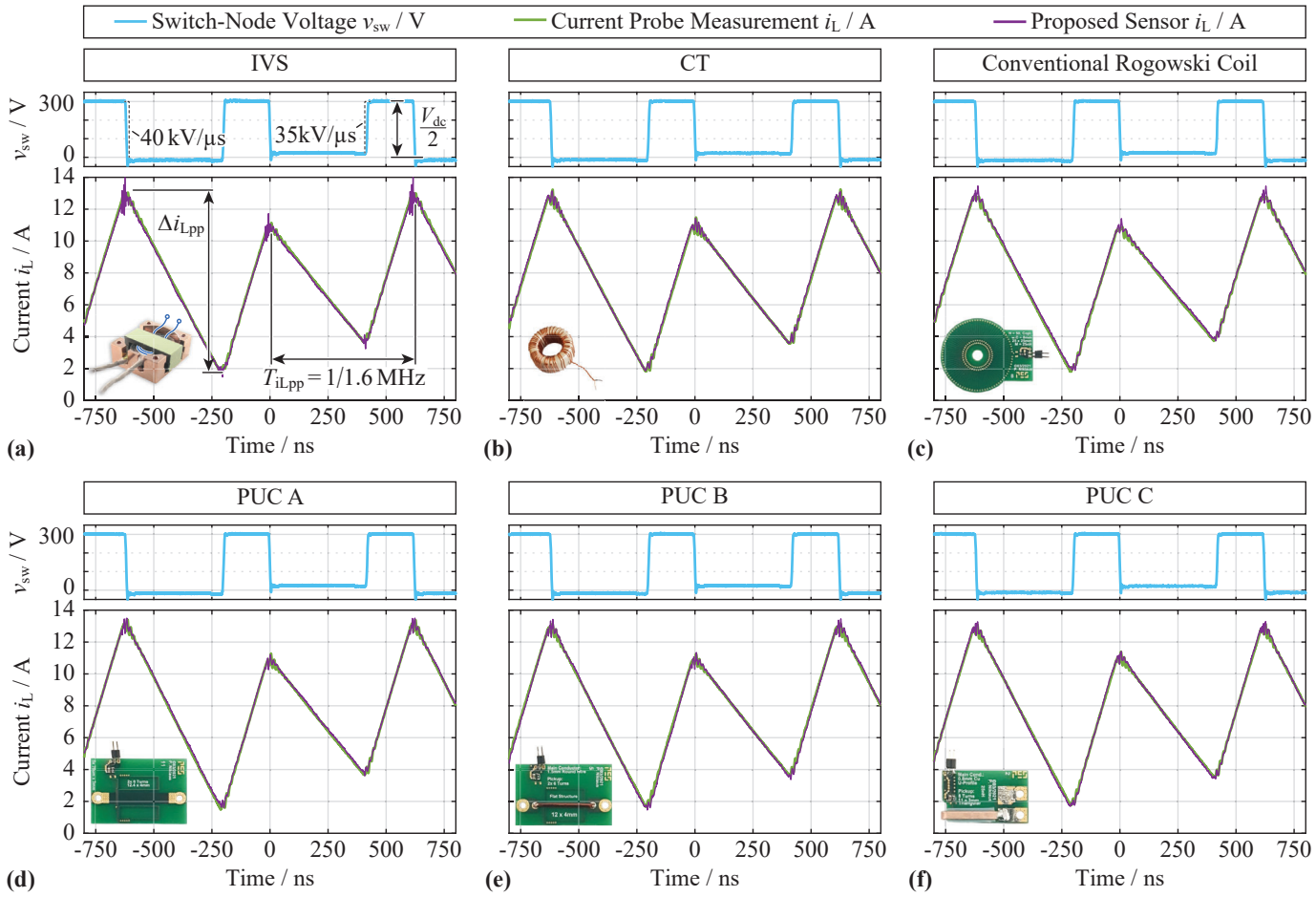

Fig. 16. Time-domain measurements of the switch-node voltage (cyan) and inductor current measured with a current probe (green) and the proposed sensors (purple) in one three-level branch of the *3L3*. Hall sensor extended with **(a)** the IVS, **(b)** the CT, **(c)** the conventional Rogowski coil, **(d)** the PUC A, **(e)** the PUC B and **(f)** the PUC C. The current measurements are placed *after* the output filter inductor at the converter output, hence the fast $\mathrm{d}v/\mathrm{d}t$ transients have no impact.

Rogowski coil/PUCs are listed in **Table II**. For the IVS it corresponds to 6.5 pF.

ii) As an approximation the coupling capacitance C_c can be split into two capacitances C_{CM1} and C_{CM2} that couple the CM disturbance into both coil terminals ① and ②. The ratio C_{CM1}/C_{CM2} depends on the layout. Consequently, the total CM current $\underline{i}_{CM} = \underline{v}_{CM}/\underline{Z}_{CM}$ divides in two parts $\underline{i}_{CM1}$ and $\underline{i}_{CM2}$, which leads to an inherent asymmetry if $C_{CM1} \neq C_{CM2}$.

iii) The differential integrator is not perfectly matched, hence even for symmetrical distribution of the CM current the two voltages $\underline{v}_p$ and $\underline{v}_n$ are not equal. Thus a CM to differential-mode (DM) conversion occurs.

iv) $\underline{v}_p$ and $\underline{v}_n$ are composed of a CM and a DM component. They lead to a CM excitation of the subsequent differential combiner circuit. The operational amplifiers only have a finite CMRR, mainly limited by the matching of the feedback network [30], hence there is a CM-to-DM conversion.

A distortion of 1 A corresponds to only 3.6 mV after the integrator for $f_{int} = 19$ kHz and $M = 30$ nH. With a CM voltage of 300 V this results in a CMRR of almost 100 dB, i.e., $1:100'000$. With error voltages that low, the distortions visible in **Fig. 17** for the conventional Rogowski coil and the PUCs cannot be broken down any further to assign certain error components to one of the above listed effects. Nevertheless, the different approaches can be compared qualitatively. Of particular interest is the comparison between the IVS and the Rogowski coil/PUCs because they rely on the same operational principle. The distortions are caused by the flowing $\underline{i}_{CM}$ and are independent of the selected coil arrangement. Assuming equal $\underline{Z}_{CM}$ in all cases, the CM distortions should be identical. For the IVS, however, there is a significantly improved signal-to-noise ratio (SNR), due to the higher mutual inductance M (≈ 2.1 µH compared to ≈ 30 nH). Please note, that noise in this context refers to the adverse CM distortion. Therefore, the same absolute CM distortion naturally has a lower effect. A further consequence of the high coupling is the lower integrator corner frequency f_{int} that can be selected for the same measurement sensitivity (cf. (6)). To maximize $\underline{Z}_{CM}$ for a given C_c, i.e., minimize $\underline{i}_{CM}$, R is ideally chosen as large as possible (cf. (12)). Consequently, for a given f_{int}, C reduces to small values. The lower limit for C is obtained by the CM voltage excitation of the amplifier inputs. Assuming a perfectly matched integrator, the CM excitation of the operational amplifiers is

$$\underline{v}_{CM,amp} = \underline{v}_{CM} \cdot \frac{C_c}{C_c + 2C} \cdot \frac{1}{1 + s \cdot \frac{R}{2} \cdot \frac{C_c \cdot 2C}{C_c + 2C}}. \qquad (13)$$

This article has been accepted for publication in IEEE Transactions on Industry Applications. This is the author's version which has not been fully edited and content may change prior to final publication. Citation information: DOI 10.1109/TIA.2022.3164865

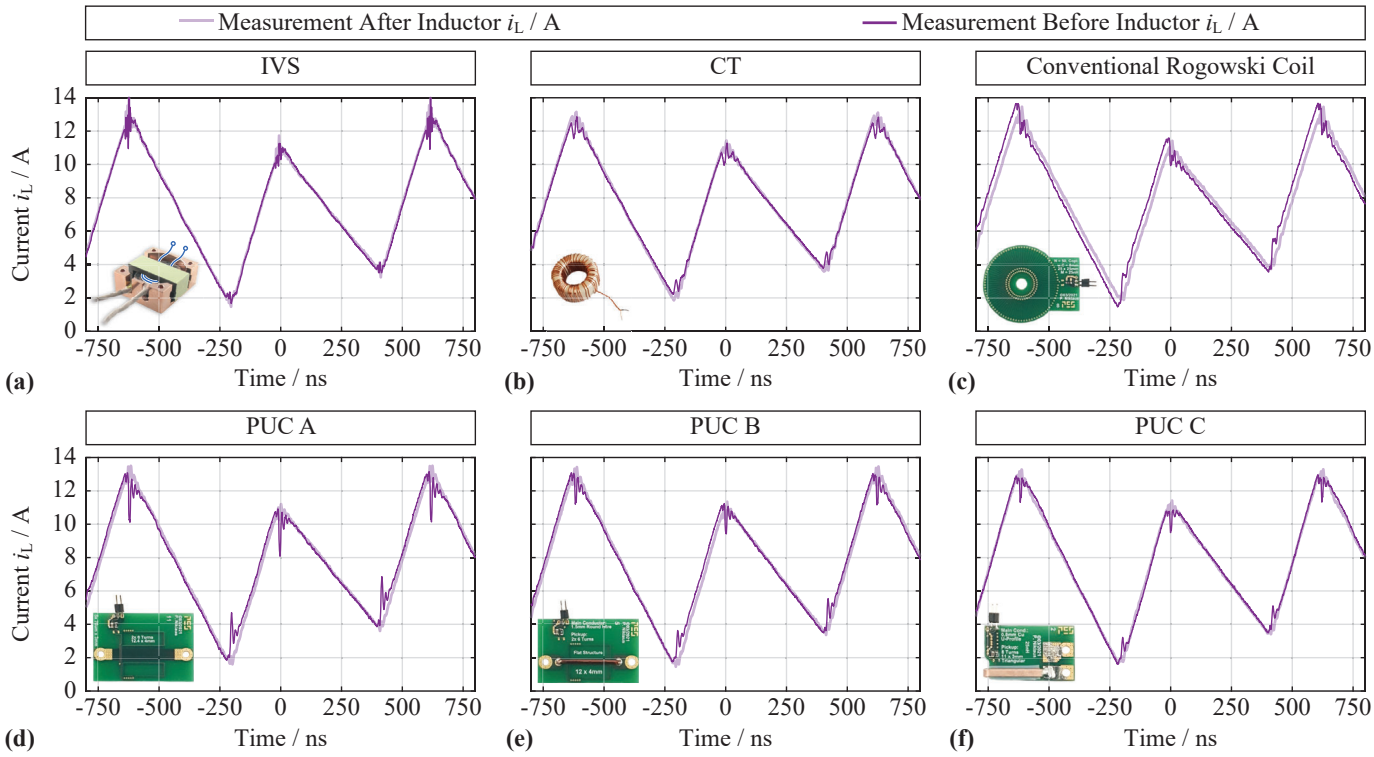

Fig. 17. Comparison between measurement before the inductor directly at the switch-node (purple) vs. measurement after the inductor as shown in Fig. 16 (light purple) for a $\mathrm{d}v/\mathrm{d}t$ between 35 and 40 $\mathrm{kV/\mu s}$. Hall sensor extended with **(a)** the IVS, **(b)** the CT, **(c)** a conventional Rogowski coil, **(d)** the PUC A, **(e)** the PUC B and **(f)** the PUC C.

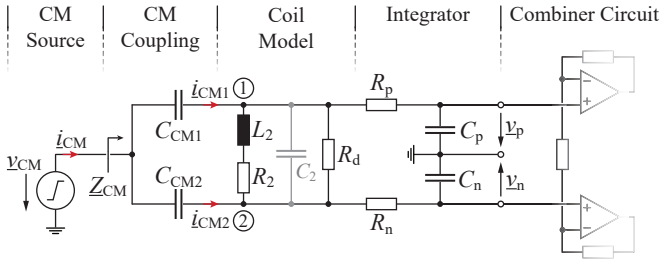

Fig. 18. CM equivalent circuit of the PUC with asymmetric coupling ($C_{\mathrm{CM1}} \neq C_{\mathrm{CM2}}$) of the CM current $\underline{i}_{\mathrm{CM}}$ into the coil and integrator.

The step response of (13) has a steady-state value of $v_{\mathrm{CM,amp},0} = v_{\mathrm{CM}} \cdot \frac{C_\mathrm{c}}{C_\mathrm{c}+2C}$. To prevent saturation of the amplifiers, $v_{\mathrm{CM,amp},0}$ must be below the maximum allowed amplifier input voltage. With the worst-case value $C_\mathrm{c} = 6.5\,\mathrm{pF}$ (IVS) and a CM voltage of $400\,\mathrm{V}$, C must be larger than $1.5\,\mathrm{nF}$ to confine $v_{\mathrm{CM,amp},0}$ to values below $0.9\,\mathrm{V}$ (limit for the considered amplifier with $\pm 2.5\,\mathrm{V}$ supply [20]). Given the minimum required C it is obvious that a lower f_{int} results in a higher R and thus a lower CM current i_{CM}. Eventually, this means a lower CM error due to effects ii) to iv) as listed above. Currently, the integrator is realized with $R = 75\,\mathrm{k\Omega}$ and $C = 6\,\mathrm{nF}$ for the IVS and with $R = 5.6\,\mathrm{k\Omega}$ and $C = 1.5\,\mathrm{nF}$ for the Rogowski coil/PUCs. With the C_c values listed in **Table II**, C could be slightly reduced to achieve a better CMRR without exceeding the maximum amplifier input voltage.

As a conclusion, the IVS, despite having the largest coupling capacitance C_c, has a significantly better CMRR thanks to the higher SNR and thanks to the lower f_{int} due to its substantially higher mutual inductance. The differences between the Rogowski coil/PUCs are very small and can be qualitatively explained with the effects ii) to iv) as listed above.

The CT is terminated with a very low-ohmic burden resistor R placed symmetrically to ground ($R/2$ from each terminal to ground). Given the very close matching of the two burden resistors, there is almost no CM-to-DM conversion occurring and the CM voltage at the amplifier inputs is very low. Furthermore, the CT can be shielded very effectively, which provides a very low impedance path for the CM current that is independent of the evaluation circuit input stage.

As a final remark it has to be mentioned that inductor current measurements are normally placed after the inductor exactly to prevent disturbing the signal with high $\mathrm{d}v/\mathrm{d}t$ transients. In this case all presented sensors are suitable for the high-BW current measurements.

VII. Comparative Evaluation and Discussion

Table IV shows a comparative evaluation of different designs presented in the literature and the investigated designs in this work. Only the best performing PUC (PUC C) is included. Different criteria such as BW, DC capability, mutual inductance M (for Rogowski based sensors), size, $\mathrm{d}v/\mathrm{d}t$-immunity and realization effort are considered. The size includes only the sensor part without processing electronics. In industrial applications more and more functionalities are fully integrated and thus the processing electronics can be realized very compact. PUC C has the highest BW of all DC capable sensors and particularly outperforms the similarly operating sensor in [14] (higher BW, smaller size thanks to the PCB realization). The CT based design of this work outperforms [7] and [9] in terms of BW and realization effort (the latter are more complex in

This article has been accepted for publication in IEEE Transactions on Industry Applications. This is the author's version which has not been fully edited and content may change prior to final publication. Citation information: DOI 10.1109/TIA.2022.3164865

TABLE IV. Comparative evaluation of the investigated designs in this work (bold) and solutions presented in literature regarding BW, DC capability, mutual inductance M, sensor size (including the Hall element or the commercial Hall-effect current sensor (CS) in case of DC capable solutions), $\mathrm{d}v/\mathrm{d}t$-immunity (qualitative; with voltage step and slope, if specified) and realization effort (qualitative). The results are grouped by DC capability and sorted by descending BW. Please note that a BW determined by simulation or calculation is indicated with † and a BW determined from the ringing in the measured waveform is indicated with ‡. n.a. = not applicable.

Ref.	BW (MHz)	DC capable	M (nH)	Coil Size / Sensor Volume (mm)	$\mathrm{d}v/\mathrm{d}t$-Immunity	Realization Effort
PUC C	$\mathbf{> 50}$	**yes**	**30**	$\mathbf{11 \times 11 \times 3}$ **(Hall CS)** $\mathbf{17 \times 4 \times 3}$ **(PUC)**	**– (300V@40kV/µs)**	**++**
CT	**35**	**yes**	**n.a.**	$\mathbf{11 \times 11 \times 3}$ **(Hall CS)** $\mathbf{13 \times 13 \times 7}$ **(CT)**	**+ (300V@40kV/µs)**	**–**
IVS	**10**	**yes**	$\mathbf{\approx 2100}$	$\mathbf{11 \times 11 \times 3}$ **(Hall CS)**	**++ (300V@40kV/µs)**	**+**
[14]	$\approx 30^{\dagger}$	yes	≈ 10	$\approx 3 \times 2 \times 1$ (Hall element) $\approx 40 \times 40 \times 2$ (coil)	not specified	+
[7]	30	yes	n.a.	$18 \times 10 \times 8$ (incl. Hall element)	+ (100V@16kV/µs)	––
[9]	20	yes	n.a.	$20 \times 20 \times 7$ (incl. Hall element)	+ (350V@16kV/µs)	––
[13]	5	yes	n.a.	$\approx 6 \times 5 \times 2$ (Hall CS) $\approx 9 \times 8 \times 6$ (CT)	not specified	++
[23]	$355^{\dagger}$	no	2.3	$\approx 4 \times 4$	not specified	++
[21]	$333^{\ddagger}$	no	0.1	$\approx 6 \times 0.1$	not specified	++
[22]	$225^{\dagger}$	no	0.1	$\approx 10 \times 3$	not specified	++
[25]	$100^{\dagger}$	no	10.7	$\approx 8 \times 8$	not specified	++
[21]	$93^{\ddagger}$	no	0.9	$\approx 6 \times 0.8$	not specified	++

realization due to the gapped magnetic core) with a similar size. The CT realization in [13] is utilizes only commercial components and has a low realization effort. However, it has the lowest BW and the compact size is only possible due to the small current range of max. ± 20 A. Therefore, this solution is not applicable for the target application. As shown before, CT based designs generally have better $\mathrm{d}v/\mathrm{d}t$-immunity compared to Rogowski based designs. One exception is the IVS, which thanks to its very high coupling and low corner frequency has the best immunity, requires no additional volume for the sensor but at the same time has the lowest BW. The IVS proposed in this work is only applicable if a dedicated custom-made filter inductor with accessible core to place the sense winding is used.

Rogowski based pickup coil sensors without DC capability are not feasible for the desired application but are still included in **Table IV** (lower part), since they serve as basis for the investigated PUCs. On the one hand, they achieve a very high BW and are highly compact with minimal realization effort (no magnetic elements, no Hall sensor) but on the other hand they typically have low values of M (a factor of 3 to 300 lower than the PUCs in this work). This is expected, since a high BW means low self-impedance and therefore small dimensions and/or a low number of turns. For a given measurement sensitivity in V/A a low M requires a high ω_{int}, which is problematic in case of desired DC capability, since eventually the condition $f_{\mathrm{Hall}} \gg f_{\mathrm{int}}$ is violated, which leads to deviations in the frequency response. Moreover, the BW of these designs is not measured directly but determined with FEM simulations or calculated based on self-impedance measurements. As summarized in **Table II** the PUC designs presented in this work have self-resonance frequencies between 100 and 200 MHz (extracted from self-impedance measurements), which indicates a BW > 50 MHz while having a much higher M.

In summary, the presented concepts exceed the performance of previously shown solutions in the literature especially concerning BW and manufacturability. A HF extension with PUC C is recommended if maximum BW and lowest realization effort is desired. The CT is advantageously used if a high $\mathrm{d}v/\mathrm{d}t$-immunity is required. In case of a physically present filter inductor with the possibility to add the sense winding the IVS is suggested, since it requires the lowest volume and has a superior $\mathrm{d}v/\mathrm{d}t$-immunity.

VIII. Conclusion

This paper analyzes approaches to extend the bandwidth (BW) of a commercially available low frequency (LF) Hall-effect current sensor beyond 10 MHz. The aim is to implement a wideband current measurement for closed-loop control of a ultra-high BW AC power source with an effective switching frequency $f_{\mathrm{sw,eff}} = 4.8$ MHz realized as three-level triple-interleaved flying capacitor converter (3L3) employing wide bandgap GaN semiconductors.

In [18], two high frequency (HF) current sensors to be used in combination with a Hall-effect current sensor are presented. First, an already present output filter inductor is equipped with an additional sense winding to obtain the inductor current by integration of the inductive voltage drop (*galvanically isolated inductor voltage sensing*, IVS). No additional volume for the HF sensor is required in this case. Second, a small current transformer (CT) with an ungapped toroidal iron powder core is used to measure the HF current, while at the same time it can handle the DC/LF bias due to the LF current. It contributes a volume of approximately 1.2 cm^3. In both cases, the secondary windings have to be manually wound, which complicates the manufacturing and makes it difficult to achieve reproducible results in practice, since the parasitic elements, which mainly define the HF performance, are difficult to control.

This work furthermore presents highly compact PCB integrated HF sensors based on a conventional circular PCB integrated Rogowski coil as alternative BW extension concepts. Compared to the IVS and CT and advantageous in industrial

applications, the manufacturability of PCB integrated components is significantly improved and the parasitics are tightly controlled.

Based on previous research in the literature, three pickup coil (PUC) geometries that offer a high magnetic coupling per area and low self parasitics are built and compared to the conventional Rogowski coil. A coil size as low as $17 \times 3.5\,\mathrm{mm}$ (HF sensor volume $\approx 0.2\,\mathrm{cm}^3$) is achieved. The transition between LF and HF current sensors is realized with a fully-differential combiner circuit whose signal processing electronics occupies only $22 \times 25\,\mathrm{mm}$.

Comprehensive experimental verification with a hardware demonstrator of a single bridge-leg of the *3L3* proves that all investigated concepts accurately represent the $1.6\,\mathrm{MHz}$ triangular current ripple. The BW of the three PUC geometries exceeds $50\,\mathrm{MHz}$ whereas the conventional Rogowski coil achieves $28\,\mathrm{MHz}$ due to its low self-resonance frequency (SRF). Compared to the IVS and CT, which reach a BW of $10\,\mathrm{MHz}$ and $35\,\mathrm{MHz}$ respectively, a substantial improvement is possible with the PUCs.

In a final step, the immunity of all six investigated concepts to common-mode (CM) disturbances (CM rejection ratio (CMRR)) resulting from fast $\mathrm{d}v/\mathrm{d}t$ transients is analyzed. Compared to the Rogowski coil and the PUCs, the IVS shows superior CMRR. It has to be emphasized, however, that the occurring error in the Rogowski coil/PUC current measurement signals corresponds to an error voltage in the mV range. With several hundred volts of CM voltage, still a CMRR of almost $100\,\mathrm{dB}$ is achieved.

With the obtained results, the IVS is suggested for current measurements in a dedicated output filter inductor if there is the possibility to access the core to place the sense winding and if the bandwidth of $10\,\mathrm{MHz}$ is acceptable because it requires no additional volume for the sensor and it offers a high CMRR. In other cases, either the CT or the PUCs are suitable and the choice depends on a trade-off between required bandwidth, space requirements, CMRR, manufacturability and realization effort. If maximum BW is desired, the PUCs are preferably selected. Comparing the three PUC designs, PUC C outperforms PUC A and PUC B in all considered performance criteria (bandwidth, volume, CMRR) and should therefore be preferred.

REFERENCES

[1] P. S. Niklaus, J. Azurza Anderson, D. Bortis, and J. W. Kolar, "Ultra-high bandwidth gan-based class-d power amplifier for testing of three-phase mains interfaces of renewable energy systems," in *Proc. of the 8th International Conference on Renewable Energy Research and Applications (ICRERA)*, 2019, pp. 615–622.

[2] F. Krismer, V. N. Behrunani, P. S. Niklaus, and J. W. Kolar, "Optimized cascaded controller design for a 10 kw / 100 khz large signal bandwidth ac power source," in *Proc. of the IEEE Energy Conversion Congress and Exposition (ECCE)*, 2020, pp. 5669–5676.

[3] E. H. Hall, "On a new action of the magnet on electric currents," *American Journal of Mathematics*, vol. 2, no. 3, pp. 287–292, 1879.

[4] Allegro Microsystems, "Acs733 – datasheet," 2020, accessed on 31.05.2021. [Online]. Available: https://www.allegromicro.com/-/media/files/datasheets/acs732-3-kla-datasheet.ashx

[5] Sensitec GmbH, "Cfs1000 – datasheet," 2020, accessed on 31.05.2021. [Online]. Available: https://www.sensitec.com/fileadmin/sensitec/Service_and_Support/Downloads/Data_Sheets/CFS1000/SENSITEC_CFS1000_DSE_05.pdf

[6] LEM International SA, "High precision current transducers," 2011, accessed on 31.05.2021. [Online]. Available: https://www.lem.com/en/file/5619/download

[7] L. Dalessandro, N. Karrer, and J. W. Kolar, "High-performance planar isolated current sensor for power electronics applications," *IEEE Transactions on Power Electronics*, vol. 22, no. 5, pp. 1682–1692, 2007.

[8] L. Ghislanzoni and J. A. Carrasco, "A dc current transformer for large bandwidth and high common-mode rejection," *IEEE Transactions on Industrial Electronics*, vol. 46, no. 3, pp. 631–636, 1999.

[9] G. Laimer and J. W. Kolar, "Wide bandwidth low complexity isolated current sensor to be employed in a 10 kw/500 khz three-phase unity power factor pwm rectifier system," in *Proc. of the 33rd IEEE Power Electronics Specialists Conference (PESC)*, vol. 3, 2002, pp. 1065–1070.

[10] J. A. Carrasco, E. Sanchis-Kilders, D. Ramirez, and E. J. Dede, "Improved magnetic coupled current sensing techniques [space power applications]," in *Proc. of the 27th IEEE Power Electronics Specialists Conference (PESC)*, vol. 1, 1996, pp. 829–834.

[11] B. Mammano, "Current sensing solutions for power supply designers," Unitrode Corp., 1997.

[12] P. Hofer-Noser and N. Karrer, *Hochdynamische Stromerfassung in der Leistungselektronik*. Springer Berlin Heidelberg, 2006, pp. 849–883.

[13] B. Ulrich, "Open-source wideband (dc to mhz range) isolated current sensor," *HardwareX*, vol. 5, 2019.

[14] N. Karrer and P. Hofer-Noser, "A new current measuring principle for power electronic applications," in *Proc. of the 11th IEEE International Symposium on Power Semiconductor Devices and ICs (ISPSD)*, May 1999, pp. 279–282.

[15] W. Rogowski and W. Steinhaus, "Die Messung der magnetischen Spannung (in German)," *Archiv f. Elektrotechnik*, vol. 1, no. 4, pp. 140–150, 1912.

[16] H. L. Votzi, M. Vogelsberger, and H. Ertl, "Low-cost current sensor for power capacitors based on a pcb rogowski-coil," in *Proc. of the International Exhibition & Conference for Power Electronics, Intelligent Motion, Power Quality (PCIM)*, 2011.

[17] B. Carsten, "The proximity current probe; obtaining wideband current waveforms in thick film and printed circuit conductors," in *Proc. of the 1st High Frequency Power Conversion Conference (HFPC)*, May 1989.

[18] P. S. Niklaus, D. Bortis, and J. W. Kolar, "High bandwidth high cmrr current measurement for a 4.8 mhz multi-level gan inverter ac power source," in *Proc. of the IEEE Applied Power Electronic Conference and Exposition (APEC)*, 2021, pp. 200–207.

[19] W. Ray and R. Davis, "Wide bandwidth rogowski current transducers part 1: The rogowski coil," *EPE Journal*, vol. 3, no. 1, pp. 51–59, 1993.

[20] Texas Instruments, "Opa859 – datasheet," 2018, accessed on 31.05.2021. [Online]. Available: https://www.ti.com/lit/ds/symlink/opa859.pdf

[21] K. Wang, X. Yang, H. Li, L. Wang, and P. Jain, "A high-bandwidth integrated current measurement for detecting switching current of fast gan devices," *IEEE Transactions on Power Electronics*, vol. 33, no. 7, pp. 6199–6210, 2018.

[22] J. Wang, M. H. Hedayati, D. Liu, S.-E. Adami, H. C. P. Dymond, J. J. O. Dalton, and B. H. Stark, "Infinity sensor: Temperature sensing in gan power devices using peak di/dt," in *Proc. of the IEEE Energy Conversion Congress and Exposition (ECCE)*, 2018, pp. 884–890.

[23] U.-J. Kim and R.-Y. Kim, "Analysis of various pickup coil designs in nonmodule-type gan power semiconductors," *Sensors*, vol. 20, no. 21, p. 6066, Oct. 2020.

[24] L. Zhao, J. van Wyk, and W. Odendaal, "Planar embedded pick-up coil sensor for power electronic modules," in *Proc. of the IEEE Applied Power Electronics Conference and Exposition (APEC)*, vol. 2, 2004, pp. 945–951 vol.2.

[25] Y. Xue, J. Lu, Z. Wang, L. M. Tolbert, B. J. Blalock, and F. Wang, "A compact planar rogowski coil current sensor for active current balancing of parallel-connected silicon carbide mosfets," in *Proc. of the IEEE Energy Conversion Congress and Exposition (ECCE)*, 2014, pp. 4685–4690.

[26] Keysight Technologies, "E4991b impedance analyzer – datasheet," 2020, accessed on 31.05.2021. [Online]. Available: https://www.keysight.com/ch/de/assets/7018-04259/data-sheets/5991-3893.pdf

[27] Omicron Lab, "Bode 100 – user manual," 2021, accessed on 31.05.2021. [Online]. Available: https://www.omicron-lab.com/fileadmin/assets/Bode_100/Manuals/Bode-100-User-Manual-ENU10060507.pdf

[28] apitech, "Fixed coaxial attenuators model 45 and model 58 – datasheet," 2020, accessed on 31.05.2021. [Online]. Available: https://www.apitech.com/globalassets/documents/i--w/data-sheet---attenuators-fixed-wmod4558.pdf

[29] Tektronix, Inc., "Tcp0030a – datasheet," 2017, accessed on 31.05.2021. [Online]. Available: https://download.tek.com/datasheet/TCP0030A-Current-Probe-Datasheet-51W1904210.pdf

[30] R. Pallas-Areny and J. G. Webster, "Common mode rejection ratio in differential amplifiers," *IEEE Transactions on Instrumentation and Measurement*, vol. 40, no. 4, pp. 669–676, Aug 1991.

Pascal S. Niklaus (STM'17) received his B.Sc. and M.Sc. degree (with distinction) in electrical engineering from the Swiss Federal Institute of Technology (ETH) Zurich, Switzerland, in 2016 and 2018, respectively. During his studies he did two internships where he developed hardware, firmware and software for custom and off-the-shelf test and measurement equipment as well as working on the firmware development for a new microprocessor architecture. In April 2018 he joined the Power Electronic Systems Laboratory (PES) at ETH Zurich as a Ph.D. student focusing on advanced measurement technologies in the field of power electronics and on high bandwidth power converters featuring wide bandgap power semiconductors.

Dominik Bortis (SM'21) received the M.Sc. and Ph.D. degree in electrical engineering from the Swiss Federal Institute of Technology (ETH) Zurich, Switzerland, in 2005 and 2008, respectively. In May 2005, he joined the Power Electronic Systems Laboratory (PES), ETH Zurich, as a Ph.D. student. From 2008 to 2011, he has been a Postdoctoral Fellow and from 2011 to 2016 a Research Associate with PES. Since January 2016 Dr. Bortis is heading the research group Advanced Mechatronic Systems at PES, which concentrates on ultra-high speed motors, bearingless drives, linear-rotary actuator and machine concepts with integrated power electronics. Targeted applications include e.g. highly dynamic positioning systems, medical systems, and future mobility concepts. Dr. Bortis has published 90+ scientific papers in international journals and conference proceedings. He has filed 30+ patents and has received 10 IEEE Conference Prize Paper Awards and 2 First Prize Transaction Paper Awards.

Johann W. Kolar (F'10) received the M.Sc. and Ph.D. degrees (summa cum laude) from the Vienna University of Technology, Vienna, Austria. He is currently a Full Professor and the Head of the Power Electronic Systems Laboratory at the Swiss Federal Institute of Technology (ETH) Zurich, Zurich, Switzerland. Dr. Kolar has proposed numerous novel converter concepts incl. the Vienna Rectifier, the Sparse Matrix Converter and the Swiss Rectifier, has spearheaded the development of x-million rpm motors, and has pioneered fully automated multi-objective power electronics design procedures. He has graduated 80+ Ph.D. students, has published 900+ journal and conference papers and 4 book chapters, and has filed 200+ patents. He has presented 30+ educational seminars at leading international conferences and has served as IEEE PELS Distinguished Lecturer from 2012 2016. He has received 40+ IEEE Transactions and Conference Prize Paper Awards, the 2014 IEEE Power Electronics Society R. David Middlebrook Achievement Award, the 2016 IEEE PEMC Council Award, the 2016 IEEE William E. Newell Power Electronics Award, the 2021 EPE Outstanding Achievement Award and 2 ETH Zurich Golden Owl Awards for excellence in teaching. He was elected to the U.S. National Academy of Engineering as an international member in 2021. The focus of his current research is on ultra-compact/efficient WBG converter systems, ANN-based design procedures, Solid-State Transformers, ultra-high speed drives, and bearingless motors.